ISTANBUL TECHNICAL UNIVERSITY ★ GRADUATE SCHOOL

MODELING OF TWO-PHASE BLOOD FLOW AND FLUID-STRUCTURE INTERACTIONS IN CEREBRAL ANEURYSMS

Ph.D. THESIS

Hamed PAHLAVANI

Department of Mechanical Engineering

Mechanical Engineering Program

NOVEMBER 2022

ISTANBUL TECHNICAL UNIVERSITY ★ GRADUATE SCHOOL

MODELING OF TWO-PHASE BLOOD FLOW AND FLUID-STRUCTURE INTERACTIONS IN CEREBRAL ANEURYSMS

Ph.D. THESIS

Hamed PAHLAVANI
(503152005)

Department of Mechanical Engineering

Mechanical Engineering Program

Thesis Advisor: Prof. Dr. İ. Bedii ÖZDEMİR

NOVEMBER 2022

ISTANBUL TEKNİK ÜNİVERSİTESİ ★ LİSANSÜSTÜ EĞİTİM ENSTİTÜSÜ

SEREBRAL ANEVRİZMALARDA İKİ-FAZLI KAN AKIŞININ VE BUNUN DAMAR DUVARLARI İLE ETKİLEŞİMLERİNİN MODELLENMESİ

DOKTORA TEZİ

Hamed PAHLAVANI
(503152005)

Makina Mühendisliği Anabilim Dalı

Makina Mühendisliği Programı

Tez Danışmanı: Prof. Dr. İ. Bedii ÖZDEMİR

KASIM 2022

Hamed PAHLAVANI, a Ph.D. student of ITU Graduate School student ID 503152005 successfully defended the thesis/dissertation entitled “MODELING OF TWO-PHASE BLOOD FLOW AND FLUID-STRUCTURE INTERACTIONS IN CEREBRAL ANEURYSM”, which he prepared after fulfilling the requirements specified in the associated legislations, before the jury whose signatures are below.

Thesis Advisor :	**Prof. Dr. İ. Bedii ÖZDEMİR** İstanbul Technical University	.....
Jury Members :	**Prof. Dr. Cem PARMAKSIZOĞLU** Istanbul Technical University	.....
	Prof. Dr. Düzgün YILDIRIM Acıbadem University	.....
	Prof. Dr. Alim Rüstem ASLAN Istanbul Technical University	.....
	Assoc. Prof. Dr. İlyas YILMAZ Istanbul Bilgi University	.....

Date of Submission : 9 November 2022
Date of Defense : 16 December 2022

To my family,

FOREWORD

This thesis is written as a completion for my PhD degree in mechanical engineering, Istanbul Technical University.

I would like to express my sincere gratitude to my supervisor Prof. Dr. İ. Bedii ÖZDEMİR for his guiding, understanding and patience he presented during my thesis work.

I would also like to thank Prof. Dr. Düzgün YILDIRIM and Prof. Dr. Cem PARMAKSIZOĞLU for their endless support, inspiration and encouragement during the several defense meetings.

I cannot begin to express my gratitude to my family for all of the love, support, encouragement and prayers they have sent my way along this journey.

November 2022

Hamed PAHLAVANI
(Mechanical Engineer)

TABLE OF CONTENTS

Page

ABBREVIATIONS

ALE	**:** Arbitrary Lagrangian Eulerian
CFD	**:** Computational Fluid Dynamics
CFL	**:** Courant Friedrichs Lewy
FSI	**:** Fluid Structure Interaction
GGI	**:** General Grid Interface
H	**:** Haematocrit
IBM	**:** Immersed Boundary Method
IQN-ILS	**:** Interface Quasi-Newton with Inverse Jacobian from a Least-squares
MULES	**:** Multidimensional Universal Limiter for Explicit Solution
OSI	**:** Oscillatory Shear Index
RBC	**:** Red Blood Cells
RBF	**:** Radial Basis Function
TAWSS	**:** Time Averaged Wall Shear Stress
WBC	**:** White Blood Cells
WSS	**:** Wall Shear Stress

SYMBOLS

$\boldsymbol{A}$: Contact area
$\boldsymbol{C_D}$: Drag coefficient
$\boldsymbol{D_s}$: Displacement vector in the solid part
$\boldsymbol{d_d}$: The diameter of RBC's
$\boldsymbol{F_{VM}}$: Virtual mass
$\boldsymbol{F_O}$: Forces like Basset force
$\boldsymbol{F_L}$: Instantaneous lift force
$\boldsymbol{F_D}$: Instantaneous drag force
$\boldsymbol{g}$: Gravitational acceleration
$\boldsymbol{I}$: Unit tensor
$\boldsymbol{m}$ and $\boldsymbol{n}$: Hematocrit functions
$\overline{\boldsymbol{M}}_{\phi}$: Average inter-phase momentum transfer term
$\overline{\boldsymbol{p}}_{\boldsymbol{d}}$: Particle pressure
$\dot{\boldsymbol{s}}$: The rate of shear strain
$\boldsymbol{tr}()$: The trace of the matrix
$\boldsymbol{U_s}$: Local solid velocity vector
$\boldsymbol{U_r}$: Slip velocity
$\overline{\boldsymbol{U}}$: Local velocity vector
$\overline{\boldsymbol{U}}_{\phi}$: Phase mean velocity
$\boldsymbol{V_d}$: Volume of the disperse phase elements
$\overline{\boldsymbol{\alpha}}_{\phi}$: Phase volume fraction
$\boldsymbol{\phi}$: Shape correction factor
$\boldsymbol{\rho}$: Density
$\boldsymbol{\xi}$: Consistency index
$\boldsymbol{\nu}$: Kinematic viscosity
$\boldsymbol{\lambda}$: Time constant
$\boldsymbol{\eta}$: Dimensionless relative mixture viscosity
$\boldsymbol{\varepsilon}$: The classical Cauchy strain tensor
$\boldsymbol{\delta}$: Kronecker delta
$\boldsymbol{\Gamma_{f,s}}$: Interface
$\boldsymbol{\Omega_s}$: Solid region
$\boldsymbol{\Omega_f}$: Fluid region
$\boldsymbol{\tau_0}$: The stress beyond a threshold level
$\boldsymbol{\mu}$: Dynamic viscosity
$\boldsymbol{\lambda_s}$: Lamé's first parameter
$\overline{\boldsymbol{\sigma}}_{\phi}$: Stress tensor

LIST OF TABLES

Page

LIST OF FIGURES

Page

MODELING OF TWO-PHASE BLOOD FLOW AND FLUID-STRUCTURE INTERACTIONS IN CEREBRAL ANEURYSMS

SUMMARY

This thesis is composed of 7 chapters, each of them dealing with different aspects of numerical tools (e.g., CFD and FSI) for prediction and assessment of cerebral aneurysm rupture. Computation fluid dynamics has been widely used to investigate the effect of single-phase blood model in the risk assessments, but no further application of two-phase blood model and FSI were available. For this reason, the thesis was proposed to evaluate further applications, with the aim of better understanding of the diseases. Rupture risk assessment can be classified as (a) Flow properties (e.g., inflow penetration depth, flow complexity and flow impingement zones) and (b) wall shear stress based hemodynamic indexes (e.g., OSI and TAWSS).

Chapter 1 is introductory and reviews the cerebral aneurysms, the mechanisms leading to the disease, and current computational tools in order to predict and assess of aneurysm rupture.

Chapter 2 gives a very deep understanding about the mathematical theory behind the single-phase, two-phase flow and FSI. Considering the non-Newtonian nature of blood, two non-Newtonian viscosity models (Casson for single-phase and Carreau–Yasuda for two-phase blood assumption) are discussed here. Then it proceeds with FSI concept where an appraisal of the FSI approach and its implementation, the governing equations regarding the single-phase blood assumption and mechanics of deformable vessel structure are discussed in detail. One of the most important aspects of this thesis is to use open-source solvers for numerical implementations. Regarding the implementation of single-phase and two-phase blood CFD analysis, OpenFOAM is used which is free and open-source software for CFD from the OpenFOAM Foundation. For the implementation of an FSI problem, the preCICE multi-physic coupling toolkit is used in order to couple OpenFOAM (FVM CFD solver) and CALCULIX (FEM structure solver). Furthermore, two wall shear stress based hemodynamic indexes (TAWSS and OSI) are introduced which can be used in order to make a bridge from numerical results to rupture risk assessments.

Two patient-specific cerebral aneurysms are given in chapter 3 where the first patient was a female of 41 years old, who had anterior communicating artery aneurysm with concomitant subarachnoid hemorrhage and left frontobasal hematoma, and the second patient was a female of 62 years old, who had dolichoectatic carotid and vertebral arteries. The 3D images in digital imaging and communications in medicine format were anatomically remodeled into patient-specific 3D geometries in the STL format. The FVM mesh, boundary conditions and numerical implementations used for CFD and FSI analysis of two aneurysms are discussed in detail in this chapter.

Chapter 4 investigates the blood transport in the cerebral aneurysm using single-phase and two-phase models. In two-phase Euler-Euler approach, the blood is represented by two interpenetrating continua where the dispersed red blood cells of non-Newtonian

characteristics are suspended in the continuous Newtonian plasma. The results of two-phase model, where the RBCs phase is assumed to be Carreau–Yasuda fluid, are validated against the experimental data. Furthermore, comparative analyses were performed in two patient-specific aneurysms, which indicated that for a given pulsatile flow rate, the two-phase blood approach has vitally advantageous over the single-phase assumption, and revealed a deeper inflow penetration, more complex flow structures and denser flow diversion zones in the aneurysm sac. It was obvious that the high OSI values calculated by the two-phase model covered much wider regions than the single-phase predicted. It was equally crucial that these regions coincided with the TAWSS values lower than the threshold that the single-phase approach can predict. Apparently, the single-phase model failed to spot sites of high rupture risk. The results were further exploited to identify the RBCs aggregation regions as, for example, the concave structures and narrow paths in the saccular aneurysms, for their possible use as the precursors of the thrombus formation.

Chapter 5 investigates the effect of variations in the haematocrit level on the blood flow in two cerebral aneurysms using the two-phase Euler-Euler approach and the Carreau–Yasuda viscosity model. The results showed that the maximum inflow jet penetration was achieved at the lowest haematocrit level, and this accompanied with strong flow impingements at the narrow corners deep inside the aneurysm sac and undesired complex flow patterns spreading from entrance to the aneurysm dome. The decrease in H level also changed the characteristics of the velocity profile inside the dome from a single- to a double-peak profile, which increased the likelihood of a daughter aneurysm formation. Furthermore, the TAWSS and OSI indicators showed that lowering the H values could change an initially low-risk case into a very high rupture risk situation. The two-phase Euler-Euler approach was used to enlighten the effect of variations in the haematocrit level to cure the blood flow issue in two cerebral aneurysms. A comprehensive description of the two-phase Euler-Euler approach and the relevant viscosity specifications were described in the previous chapter. The same patient specific aneurysms and the numerical implementations of the two-phase model discussed before were used here. However, this chapter presents an appraisal of the approach and interpretations of the flow complexity, features of the inflow diversion zone, penetration depths and the shear stress parameters based on varying Hematocrit values.

Chapter 6 investigates dynamics of the wall movements of a patient-specific aneurysm dome using the interactions of the non-Newtonian blood flow and the deformable vessels. The patient under consideration had an anterior communicating artery aneurysm with a concomitant subarachnoid hemorrhage and left frontonasal hematoma. A finite volume CFD solver was used with a 3D mesh of roughly 300000 cells and three boundary patches; the inlet, deformable walls and outlets. A linear elastic material model was considered for the deformation of the aneurysm wall and, in the structural computations, a finite element solver was employed with a solid domain of approximately 12000 elements. An open-source code was exploited for the coupling between the CFD and finite element solvers. Results showed that at the peak systole, the vortical structure of the flow in the aneurysm dome was complicated. Furthermore, the instabilities in the flow field produced intense shear forces, due to which a possible weakening of the wall material will certainly lead to an increase in the risk of the rupture and bleeding. The non-uniformity of the flow field acquired large values of the von Mises stresses, resulting in prominent wall displacements, which also matched to the high OSI and low TAWSS values. The maximum

displacements exhibited a non-stationery movement everywhere in the dome though mostly remained in the region of the impingement.

And finally, chapter 7 covers conclusions and remarks respectively.

SEREBRAL ANEVRİZMALARDA İKİ-FAZLI KAN AKIŞININ VE BUNUN DAMAR DUVARLARI İLE ETKİLEŞİMLERİNİN MODELLENMESİ

ÖZET

Bu tez, her biri serebral anevrizma bozukluğunun değerlendirilmesi ve tahmini için sayısal araçların (örneğin, CFD ve FSI) farklı yönleriyle ilgilenen 7 bölümden oluşmaktadır. Hesaplamalı Akışkanlar Dinamiği, yaygın bir şekilde risk değerlendirmelerinde tek fazlı kan modelinin etkisini araştırmak için kullanılmıştır, ancak iki fazlı kan modeli ve FSI'ın başka bir uygulaması mevcut değildir. Bu nedenle, hastalıkların daha iyi anlaşılması amacıyla ileri uygulamaların değerlendirilmesi için bu tez önerilmiştir. Yırtılma riski değerlendirmesi, (a) Akış özellikleri (örn. Sızıntı akışın nüfuz derinliği, akışın karmaşıklığı ve akışın vurma bölgeleri) ve (b) duvar kayma gerilimine dayalı hemodinamik indeksler (örn., OSI ve TAWSS) olarak sınıflandırılabilir.

Bölüm 1 giriş niteliğindedir ve serebral anevrizmaları, hastalığa yol açan mekanizmaları ve anevrizmaya bağlı yırtılmayı tahmin etmek ve değerlendirmek için mevcut hesaplama araçlarını gözden geçirir, yapılan çalışmaların amacı, içerikleri ve birbirleri ile bağlantıları açıklanmış, getirilen yeniliklerden bahsedilmiştir.

Bölüm 2, tek fazlı, iki fazlı akış ve FSI'ın arkasındaki matematiksel teori hakkında çok derin bir anlayış sağlar. Kanın Newtonyen olmayan doğası göz önüne alındığında, burada Newtonyen olmayan iki viskozite modeli (tek fazlı için Casson ve iki fazlı kan varsayımı için Carreau-Yasuda) tartışılır. Ardından, FSI yaklaşımının ve uyarlamasının değerlendirildiği, tek fazlı kan varsayımına ilişkin yönetim denklemlerinin ve deforme olabilen damar yapısının mekaniğinin ayrıntılı olarak tartışıldığı FSI konsepti ile ilerler. Bu tezin en önemli yönlerinden biri, sayısal uygulamalar için açık kaynaklı çözücüler kullanmaktır. Tek fazlı ve iki fazlı kan CFD analizinin uygulanmasına ilişkin, CFD için OpenFOAM Foundation'dan ücretsiz ve açık kaynaklı yazılım olan OpenFOAM kullanılmaktadır. Bir FSI probleminin uyarlanması adına, OpenFOAM (FVM CFD çözücü) ve CALCULIX'i (FEM yapı çözücü) birleştirmek için preCICE multifizik bağlaşım araç kiti kullanılır. Ayrıca, sayısal sonuçlardan yırtılma riski değerlendirmelerine bir köprü oluşturmak için kullanılabilecek iki duvar kesme gerilimi tabanlı hemodinamik indeks (TAWSS ve OSI) tanıtılmıştır.

Birinci hastanın subaraknoid kanama ve sol frontobazal hematom ile birlikte anterior komünikan arter anevrizmanın eşlik ettiği 41 yaşında bir kadın olduğu, ikinci hastanın dolikoektatik karotis ve vertebral arterleri olan 62 yaşında bir kadın olduğu, iki hastaya serebral anevrizma 3. bölümde verilmiştir. Dijital görüntüleme ve tıp formatındaki iletişimlerdeki 3B görüntüler, STL formatında hastaya özel 3B geometrilere anatomik olarak yeniden modellendi. İki anevrizmanın CFD ve FSI analizi için kullanılan FVM çözüm ağı, sınır koşulları ve sayısal uygulamaları bu bölümde ayrıntılı olarak tartışılmaktadır.

Bölüm 4, tek fazlı ve iki fazlı modeller kullanarak serebral anevrizmadaki kanın taşınımını araştırmaktadır. İki fazlı Euler-Euler yaklaşımında, kan, Newtonyen olmayan özelliklere sahip dağılmış kırmızı kan hücrelerinin sürekli Newton plazmasında askıya alındığı iki iç içe geçen süreklilikler ile temsil edilir. Kırmızı Kan Hücresi (KKH) fazının Carreau-Yasuda sıvısı olduğu varsayılan iki fazlı modelin sonuçları, deneysel verilere karşı doğrulanmıştır. İki fazlı model tarafından hesaplanan yüksek OSI değerlerinin, tek fazlı tahmin edilenden çok daha geniş bölgeleri kapsadığı açıktı. Bu bölgelerin tek fazlı yaklaşımın tahmin edebileceği eşiğin altındaki TAWSS değerleriyle çakışması da aynı derecede önemliydi. Görünüşe göre tek fazlı model, yüksek yırtılma riski olan yerleri tespit edemedi. Sonuçlar, örneğin, pıhtı oluşumunun öncüleri olarak olası kullanımları için, örneğin sakküler anevrizmalardaki içbükey yapılar ve dar yollar gibi RBC'lerin kümelenme bölgelerini tanımlamak için ayrıca kullanıldı.

Beşinci bölüm, iki fazlı Euler-Euler yaklaşımı ve Carreau-Yasuda viskozite modeli kullanılarak iki serebral anevrizmada hematokrit seviyesindeki değişikliklerin kan akışı üzerindeki etkisini araştırmaktadır. Sonuçlar, maksimum jet girişinin en düşük hematokrit seviyesinde elde edildiğini ve buna anevrizma kesesinin derinliklerindeki dar köşelerde güçlü akış çarpmalarını ve girişten anevrizma kubbesine yayılan istenmeyen karmaşık akış paternlerinin eşlik ettiğini gösterdi. Ayrıca H seviyesindeki azalma kubbe içindeki hız profilinin karakterini tek tepe profilinden çift tepe profiline değiştirmiş ve bu da yavru anevrizma oluşma olasılığını artırmıştır. Ayrıca, TAWSS ve OSI göstergeleri, H değerlerinin düşürülmesinin başlangıçta düşük riskli bir durumu, çok yüksek bir yırtılma riski durumuna dönüştürebileceğini göstermiştir. İki evreli Euler-Euler yaklaşımı, iki serebral anevrizmadaki kan akışı sorununu iyileştirmek için hematokrit seviyesindeki değişikliklerin etkisini aydınlatmak için kullanıldı. İki fazlı Euler-Euler yaklaşımının kapsamlı bir açıklaması ve ilgili viskozite spesifikasyonları önceki bölümde açıklanmıştır. Aynı hastaya özgü anevrizmalar ve daha önce tartışılan iki fazlı modelin sayısal uygulamaları burada kullanılmıştır. Bununla birlikte, bu bölüm, değişen Hematokrit değerlerine dayalı olarak akış karmaşıklığı, içeri akış saptırma bölgesinin özellikleri, penetrasyon derinlikleri ve kesme gerilimi parametrelerinin yaklaşımı ve yorumlarının bir değerlendirmesini sunar.

Bölüm 6, Newton tipi olmayan kan akışı ve deforme olabilen damarların etkileşimlerini kullanarak hastaya özel bir anevrizma kubbesinin duvar hareketlerinin dinamiklerini araştırır. Söz konusu hasta eşlik eden subaraknoid kanama ve sol frontonazal hematom ile birlikte anterior komünikan arter anevrizmasına sahipti. Kabaca 300000 hücre ve giriş, deforme olabilen duvarlar ve çıkışlar gibi üç sınır yamasından oluşan bir 3B çözüm ağı ile sonlu hacimli bir CFD çözücüsü kullanıldı. Anevrizma duvarının deformasyonu için doğrusal bir elastik malzeme modeli düşünüldü ve yapısal hesaplamalarda, yaklaşık 12000 elementten oluşan katı bir hesaplama alanı ile bir sonlu eleman çözücüsü kullanıldı. CFD ve sonlu eleman çözücüler arasındaki bağlantı için bir açık kaynak koddan yararlanıldı. Sonuçlar, zirve sistolde, anevrizma kubbesindeki akışın girdap yapısının karmaşık olduğunu gösterdi. Ayrıca, akış alanındaki kararsızlıklar, duvar malzemesinin olası bir zayıflamasının kesinlikle yırtılma ve kanama riskinde bir artışa yol açacağından dolayı yoğun kesme kuvvetleri üretti. Akış alanının düzensizliği, yüksek OSI ve düşük TAWSS değerleriyle eşleşen belirgin duvar yer değiştirmeleriyle sonuçlanan, von Mises gerilmelerinin büyük değerlerini elde etti. Maksimum yer değiştirmeler, çoğunlukla

çarpma bölgesinde kalmasına rağmen, kubbenin her yerinde durağan olmayan bir hareket sergiledi.

Son olarak, 7. bölüm sırasıyla sonuçları ve yorumları içermektedir.

1. INTRODUCTION

It has been known that the vascular endothelium acts as a protective dynamic interface between blood and the vessel wall [1], but deteriorates under long exposures to extreme shear conditions. As a result, the wall starts to deform and forms a balloon in the weakened area in a blood vessel. This phenomenon is named cerebral aneurysm (variously called an intracranial aneurysm). A cerebral aneurysm is a weakened region on the wall of an artery in the brain, where an abnormal bulging happens due to the mutual exchange of momentum between the blood flow and arterial walls. The strong shear due to abnormal blood pressure, combined with genetic predisposition, leads to the formation of focal dilation and eventually extremely thin spots [2,3]. Hence, there is always a risk of rupture and internal bleeding in such regions in 3 to 5% of the population [4]. The mechanisms leading to the formation of an aneurysm clearly requires a better understanding of the blood flow in arteries, which involves time-dependent complex physics with several cyclic steps that recirculate the oxygen, carbon dioxide and nutrients in the body [5,6]. We know that the characteristics of the flow highly depend on the transport properties of the blood, which itself is a multicomponent fluid consisting of four main components: Platelets, white blood cells (WBCs), red blood cells (RBCs) and plasma where the latter two makes up about 96% of human blood volume. The ratio of the volume of the RBCs to the volume of whole blood is called haematocrit (H), whose normal range differs from H41% to H50% for a healthy man and H36% to H45% for a woman. However, it has been known that the percentage of the RBCs can change dramatically, affecting human health condition in a negative way [7–9]. Haemoglobin, the main component of RBC, is the iron-rich protein that transports oxygen from the lungs to the rest of body tissues and takes the carbon dioxide back to the lungs. Anemia is the condition when the body does not have enough RBCs (low haematocrit) and the patient may suffer from haemoglobin deficiency, inadequate oxygen supply to the tissues and excessive bleeding where patient with haematocrit level less than H30% are exposed to high mortality risk [10]. The presence of excessive number of RBCs in the blood (high haematocrit) is called

polycythemia, which can increase the viscosity, reduce the recirculation capacity and raise the risk of thrombus formation [11].

With the advancement of computer technology, however, the computational fluid dynamics (CFD) approach has offered a significant improvement in identifying the connection between blood flow and the disease, leading to better diagnosis and treatment of the intracranial aneurysm. Flow properties such as the complexity of velocity, pressure and shear fields as well as the rate of inflow and the size and shape of the impingement zone can be obtained from the blood flow CFD analysis, which are then used to assess the aneurysm rapture risks [12]. It is clear that the blood flow CFD analysis must consider the blood as a multicomponent multiphase fluid, which consists of red and white blood cells, platelets and plasma. Biological and clinical studies indicate that the red blood cells (RBCs) are the essential constituent of blood clotting though their continuous aggregation often causes thrombus formation [13] which is frequent in large size aneurysms [14].

Hence, depending on the level of complexity of the analysis, a three-dimensional multicomponent, multiphase transport model [15–17] is required to define the blood dynamics, although the single-phase assumption has also been widely used [12,18,19]. Furthermore, one needs to take into account the shear thinning property of the blood in which the viscosity has to take into account case-dependent features of plasma and RBCs and, thus, consider the hematocrit rate, RBCs aggregations and local flow properties such as shear rate and temperature [20,21]. When the single-phase non-Newtonian assumption is used, the shear thinning behaviour of blood has been modelled using Casson or Bird-Carreau correlation [22,23]. In that, the flow is considered as a blend of the plasma and the RBCs and, thus, the viscosity of blood is determined by the viscosities of the Newtonian continuous phase (plasma) and the non-Newtonian dispersed phase (RBCs) [15,24].

Furthermore, the Fluid Structure Interaction (FSI) technique seems to provide significantly valuable information on the interactions of the blood flow and the vessel wall. Hence, using the FSI approach we can solve the equations of the blood flow and the deformable vessels using either monolithic approach with a single solver [25] or partitioned methods where two separate solvers are used for the flow and the structure [26]. Although the latter approach produces reasonably precise results, it is computationally slow due to expensive data transfer procedure. Experience, however,

shows that the convergence checks at the end each time step makes it ideal for use in the context of cerebral aneurysms, in that three-dimensional Navier-Stokes equations and linear elastic model can be used for the modeling of non-Newtonian blood flow and the vessel deformation, respectively. The FSI on the other hand, brings further intricacy due to the implementation of mesh motion, where the Immersed boundary method (IBM) and the Arbitrary Lagrangian Eulerian (ALE) appear to be the two prevailing options. The idea behind the IBM is based on solving the fluid equations for a fixed background mesh [27]. In the ALE method, however, the conditions at the fluid-solid interface are treated in the discretized equations as if the physical conditions. Thus, the fact that a change in flow field or deformation in solid phase will distort the interface [28] requires a dynamic mesh concept.

For the implementation of an FSI problem, two open-source coupling libraries are available in the literature: The first one is the FSI solvers already imbedded in the extensions of the open-source code OpenFOAM, e.g. fsiFoam and solids4Foam [29,30]. The other one is to use the preCICE multi-physics coupling toolkit [31–33]. Both libraries are ALE based FSI toolkits which enable strong coupling algorithms such as the IQN-ILS (Interface Quasi-Newton with Inverse Jacobian from a Least-squares) acceleration [34] and Aitken acceleration [35,36], where IQN-ILS leads to a faster convergence in both tools. Among the various data mapping techniques offered by the solids4Foam, e.g., directMap, Radial Basis Function (RBF) and General Grid Interface (GGI), the directMap can lead to a better convergence, but one needs to avoid non-conformal fluid-solid meshes at the coupling interface. Aneurysms however involve very complex geometries, where the spatial discretization inevitably results in the tetra-mixed non-conformal meshes. Under these circumstances, a better mapping method than the solids4Foam offers needs to be used. The preCICE, on the other hand, offers the Nearest Neighborhood and the Nearest Projection mappings [37]. The Nearest Neighbor is a first order method, beneficial in terms of computational time and ease of use, but better suited to stationery meshes. The Nearest Projection is, however, a second order method, in which the data was projected onto the mesh elements and interpolated before transforming to the other side. Despite the higher computational cost, the Nearest Projection overweights the Nearest Neighbor in terms of numerical accuracy. Hence, the use of both techniques appears to be the most proper mapping method.

1.1 Purpose of Thesis

The purpose of this thesis can be divided in three sections. First, the CFD approach was used to compare the single- and two-phase treatments of the blood flow in two cerebral aneurysms. A quick summary of the single-phase flow theory is given here and then a comprehensive description of the two-phase approach and the relevant viscosity specifications. It also includes the validation results of the two-phase method against an experimental data. Plus, we describe the patient-specific aneurysm cases and the numerical implementations of the two-phase model. This study presents an appraisal of the approach and interpretations of the flow complexity, features of the inflow diversion zone, penetration depths and the shear stress parameters such as the TAWSS and OSI.

Second, the two-phase Euler-Euler approach is used to enlighten the effect of variations in the haematocrit level to cure the blood flow issue in two cerebral aneurysms. It presents an appraisal of the approach and interpretations of the flow complexity, features of the inflow diversion zone, penetration depths and the shear stress parameters.

Finally, it presents an appraisal of the FSI approach and its implementation. A quick summary of the particulars of the FSI application is given here where we discussed interpretations of the flow complexity, features of the inflow diversion zone and penetration depths with emphasis on the shear stress parameters.

2. THEORY OF SINGLE-PHASE, TWO-PHASE AND FLUID-STRUCTURE INTERACTIONS

This chapter gives a very deep understanding about the mathematical theory behind the single-phase and two-phase blood assumptions. Considering the non-Newtonian nature of blood, two non-Newtonian viscosity models (Casson for single-phase and Carreau–Yasuda for two-phase blood assumption) are discussed here. Then it proceeds with FSI concept where an appraisal of the FSI approach and its implementation, the governing equations regarding the single-phase blood assumption and mechanics of deformable vessel structure are discussed in detail. One of the most important aspects of this thesis is to use open-source solvers for numerical implementations. Regarding the implementation of single-phase and two-phase blood CFD analysis, OpenFOAM is used which is free and open-source software for CFD from the OpenFOAM Foundation. For the implementation of an FSI problem, the preCICE multi-physic coupling toolkit is used in order to couple OpenFOAM (FVM CFD solver) and CALCULIX (FEM structure solver). Furthermore, two wall shear stress based hemodynamic indexes (TAWSS and OSI) are introduced which can be used in order to make a bridge from numerical results to rupture risk assessments.

2.1 Single-Phase Treatment of Blood Flow

2.1.1 Governing equations

The simplest approach for the motion of blood in artery vessels is to assume a single-phase flow. Surely, this is a very bold modelling and although it is computationally fast and requires low memory, it neglects fluid physics associated with the two-phase nature of the blood. Yet it has been common to use it to compare the effectiveness of the model parameters with those in the two-phase calculations. Considering incompressible laminar blood flow, three-dimensional equations for continuity and momentum transport can be written as,

$$\boldsymbol{\nabla} \cdot \boldsymbol{U}_f = 0 \tag{2.1}$$

$$\frac{D\boldsymbol{U_f}}{Dt} = -\frac{1}{\rho}\boldsymbol{\nabla}\, p + \boldsymbol{\nabla}\cdot\boldsymbol{\tau} + \boldsymbol{g} \tag{2.2}$$

where $\boldsymbol{U_f}$ is the local fluid velocity vector, p is the pressure, ρ represents the density of the blood and $\boldsymbol{\tau}$ denotes the stress tensor,

$$\boldsymbol{\tau} = p\boldsymbol{\delta} + \nu\left[\boldsymbol{\nabla U_f} + \left(\boldsymbol{\nabla U_f}\right)^T\right] - \frac{2}{3}\nu\, \boldsymbol{I\nabla}\cdot\boldsymbol{U_f} \tag{2.3}$$

here $\boldsymbol{I}$ denotes the unit tensor, $\boldsymbol{\delta}$ represents the Kronecker delta function and $(\,)^T$ denotes the transpose of the matrix. The last term in equation 2.2 represents the gravitational acceleration.

2.1.2 Non-Newtonian Viscosity of Single-Phase Blood Flow Model

Regarding the non-Newtonian fluid behaviour, the Casson correlation is exploited, which is a basic viscosity model used in blood rheology with the specified minimum and maximum viscosities ($\boldsymbol{\nu_{min}}$ and $\boldsymbol{\nu_{max}}$). In this model, the viscosity can be described by a square-root relationship provided that the stress is beyond a threshold level τ_0,

$$\nu = \left(\sqrt{\tau_0/\,\dot{s}} + \sqrt{\xi}\,\right)^2 \qquad \nu_{\min} < \nu < \nu_{\max} \tag{2.4}$$

Here $\boldsymbol{\xi}$ refers the consistency index and $\dot{\boldsymbol{s}}$ is the rate of shear strain defined as $\dot{\boldsymbol{s}} = \sqrt{\boldsymbol{2S}:\boldsymbol{S}}$ where $\boldsymbol{S} = \boldsymbol{\nabla}\overline{\boldsymbol{U_f}} + \left(\boldsymbol{\nabla}\overline{\boldsymbol{U_f}}\right)^{\boldsymbol{T}}$, and the overbar $\overline{(\,)}$ is the ensemble average over a cardiac cycle. Model constants used in this study are given in Table 2.1.

Table 2.1 : Constants used in the Casson blood viscosity model.

Parameter	Value
ξ	3.934986×10^{-6}
τ_0	2.9032×10^{-6}
ν_{max}	13.3333×10^{-6}
ν_{min}	3.9047×10^{-6}

2.2 Two-Phase Treatment of Blood Flow

2.2.1 Euler-Euler method

Contrary to the single-phase assumption, in reality the plasma is the liquid component of the blood, which holds the dispersed RBCs and other constituents

in suspension throughout the blood vessels. This means that one should consider the effects of the RBCs in the continuous plasma liquid. The Euler – Euler method [38,39] assumes that the dispersed RBCs behave like a fluid, which avoids tracking the particles, reducing the numerical cost particularly in real world situations where the Lagrangian particle tracking is almost impossible. Hence, this model can indeed be considered as a two-component flow, in that the dispersed and continuous phases are treated as two co-existing continua. The concept of phase (or component) volume fraction ($\bar{\boldsymbol{\alpha}}_{\phi}$) is introduced to describe the phase transport, where the sum of phase fractions at each location is equal to one

$$\sum \bar{\alpha}_{\phi} = 1 \tag{2.5}$$

where ϕ refers c (plasma - continuous phase) and d (RBCs - disperse phase). Hence, two sets of transport equations need to be solved simultaneously for each phase. In this study, we will ignore the enthalpy changes (with an isothermal flow assumption) and, due to low Mach and flow Reynolds (Re < 500) numbers, we will assume an incompressible laminar flow. For flows with no phase change, the phase transport equation can be written as [24],

$$\frac{\partial \bar{\alpha}_{\phi}}{\partial t} + \boldsymbol{\nabla} \cdot \left(\bar{\alpha}_{\phi} \overline{\boldsymbol{U}}_{\phi}\right) = 0 \tag{2.6}$$

where $\overline{\boldsymbol{U}}_{\phi}$ the phase mean velocity. Summing equation (2.6) written for two phases leads to continuity equation,

$$\boldsymbol{\nabla} \cdot \overline{\boldsymbol{U}} = 0 \tag{2.7}$$

where $\overline{\boldsymbol{U}} = \bar{\alpha}_c \overline{\boldsymbol{U}}_c + \bar{\alpha}_d \overline{\boldsymbol{U}}_d$. The momentum transport is given as,

$$\frac{\partial \bar{\alpha}_{\phi} \overline{\boldsymbol{U}}_{\phi}}{\partial t} + \boldsymbol{\nabla} \cdot \left(\bar{\alpha}_{\phi} \overline{\boldsymbol{U}}_{\phi} \overline{\boldsymbol{U}}_{\phi}\right) = -\frac{\bar{\alpha}_{\phi}}{\bar{\rho}_{\phi}} \boldsymbol{\nabla} \overline{p} + \boldsymbol{\nabla} \cdot \overline{\boldsymbol{\sigma}}_{\phi} + \bar{\alpha}_{\phi} \boldsymbol{g} + \frac{\overline{\boldsymbol{M}}_{\phi}}{\bar{\rho}_{\phi}} \tag{2.8}$$

where $\boldsymbol{g}$ denotes gravitational acceleration and $\overline{\boldsymbol{\sigma}}_{\phi}$ refers the stress tensor which is given for the plasma phase,

$$\overline{\boldsymbol{\sigma}}_c = \bar{\alpha}_c \nu_c \left[\boldsymbol{\nabla}\overline{\boldsymbol{U}}_c + \left(\boldsymbol{\nabla}\overline{\boldsymbol{U}}_c\right)^T\right] - \frac{2}{3}\bar{\alpha}_c \nu_c \, \boldsymbol{I}\boldsymbol{\nabla}\cdot\overline{\boldsymbol{U}}_c \tag{2.9.a}$$

and for RBCs phase,

$$\overline{\boldsymbol{\sigma}}_d = -\overline{p}_d\boldsymbol{\delta} + \bar{\alpha}_d \nu_d \left[\boldsymbol{\nabla}\overline{\boldsymbol{U}}_d + \left(\boldsymbol{\nabla}\overline{\boldsymbol{U}}_d\right)^T\right] - \frac{2}{3}\bar{\alpha}_d \nu_d \, \boldsymbol{I}\boldsymbol{\nabla}\cdot\overline{\boldsymbol{U}}_d \tag{2.9.b}$$

where δ refers the Kronecker delta, $\boldsymbol{I}$ denotes the unit tensor. ν_c and ν_d are the viscosities of the plasma and the RBCs, respectively. $\overline{p}_d$ is the particle pressure, which is assumed negligibly small within the hematocrit values considered in the present investigation [15]. Finally, in the last term, $\overline{\boldsymbol{M}}_\phi$ represents the average inter-phase momentum transfer term, whose instantaneous value can be written as,

$$\frac{\boldsymbol{M}_\phi V_d}{\alpha_d} = \boldsymbol{F}_D + \boldsymbol{F}_L + \boldsymbol{F}_{VM} + \boldsymbol{F}_O \tag{2.10}$$

Here V_d denotes the volume of the disperse phase elements, $\boldsymbol{F}_D$ represents instantaneous drag force, $\boldsymbol{F}_L$ lift, $\boldsymbol{F}_{VM}$ virtual mass and $\boldsymbol{F}_O$ other forces like the Basset force [40]. It is known [24] that the other momentum transfer mechanisms are negligible compared to the interfacial drag force, which is retained and given as

$$\boldsymbol{F}_D = \frac{1}{2}\rho_c A C_D |\,\boldsymbol{U}_r|\,\boldsymbol{U}_r \tag{2.11}$$

where $\boldsymbol{U}_r = \boldsymbol{U}_d - \boldsymbol{U}_c$ is the slip velocity, A and C_D are the contact area and the drag coefficient, respectively. The formulation closes with the Schiller – Naumann drag model [41,42],

$$C_D = \begin{cases} \frac{24}{\mathrm{Re}}\left(1 + 0.15\,\mathrm{Re}_s^{0.687}\right) & \text{if} \quad \mathrm{Re}_s < 1000 \\ 0.44 & \text{if} \quad \mathrm{Re}_s > 1000 \end{cases} \tag{2.12}$$

where $\mathrm{Re}_s = \frac{\rho_c d_d |\boldsymbol{U}_d - \boldsymbol{U}_c| \phi}{\mu_c}$; d_d being the diameter of RBC's and ϕ the shape correction factor, which brings the dependence on the shape of the disperse phase element. In this study, for the sake of simplicity, we use the formulation for a sphere in continuous flow and, thus, ϕ is set to 1.

2.2.2 Non-Newtonian viscosity of two-phase blood flow model

It is obvious that the thermophysical properties of the two-phase flow are based on a completely different constitutive structure than a single-phase flow system. Since the blood is the mixture of plasma and RBCs, the viscosity of blood must be determined as a combination of their viscosities, in that the RBCs phase, which exhibits a shear-thinning non-Newtonian fluid behaviour in shear flows, is in constant interaction with the Newtonian plasma flow. The plasma contains about 92% water and its density and viscosity can be set as 1060 kg/m^3 and 0.0011 Pa.s, respectively. Hence, the traditional non-Newtonian viscosity model of Casson [15], which is lacking an appropriate non-Newtonian viscosity model complying with the rheology of the RBCs, cannot be used in the two-phase blood flow modeling. However, the Carreau-Yasuda viscosity model can be further modified to describe the shear-thinning behavior of blood flow in which the RBCs viscosity can be extracted from dimensionless mix viscosity [15]. Considering, μ_d and μ_c as the viscosities of the RBCs and plasma, the dimensionless relative mixture viscosity η was defined as,

$$\eta = \frac{\alpha_d\,\mu_d + \alpha_c\,\mu_c}{\mu_c} = m[1 + (\lambda\dot{s})^2]^{(n-1)/2} \tag{2.13}$$

where λ denotes the time constant, which was set at 0.11 s [43], m and n are the hematocrit functions and, if the shear rate $\dot{s} > 6$ then,

$$n = 0.8092\,\alpha_d^3 - 0.8246\,\alpha_d^2 - 0.3503\,\alpha_d + 1 \tag{2.14}$$

$$m = 122.28\,\alpha_d^3 - 51.213\,\alpha_d^2 + 160305\,\alpha_d + 1 \tag{2.15}$$

and, if $\dot{s} < 6$ then,

$$\frac{(n-1)}{k_0} = -0.8913\,\alpha_d^3 + 2.0679\,\alpha_d^2 - 1.7814\,\alpha_d \tag{2.16}$$

$$m = 70.782\,\alpha_d^3 - 22.454\,\alpha_d^2 + 9.7193\,\alpha_d + 1 \tag{2.17}$$

$$k_0 = \ln\{\ln[1 + (\lambda\dot{s})^2]\}/\ln[1 + (\lambda\dot{s})^2] \tag{2.18}$$

Next, we will show the performances of the two-phase flow approach and the relevant viscosity correlation (Carreau-Yasuda) in modelling the behavior of the RBCs.

2.3 Modeling of Fluid-Structure Interaction

2.3.1 Governing equations

In order to take into account, the continuous interactions of the non-Newtonian blood flow with the living tissues of the wall through the interface, $\Gamma_{f,s}$, (see Figure 3.1) there must exist a frequent data exchange between the fluid region (Ω_f) and the solid domain (Ω_s). Hence, the interactions were embodied with the compliance conditions at the wet-surface, in that the flow velocity must be equal to the velocity of the boundary,

$$U_{f,\Gamma} = U_{s,\Gamma} \tag{2.19}$$

which is known as the kinematic continuity. Similarly, the surface stress calculated at both fluid and solid part of the interface should be equal,

$$\boldsymbol{\sigma}_{s,\Gamma} \cdot \boldsymbol{n}_{s,\Gamma} = -\boldsymbol{\sigma}_{f,\Gamma} \cdot \boldsymbol{n}_{f,\Gamma} \tag{2.20}$$

which is called the dynamic continuity and entails

$$\boldsymbol{n}_{s,\Gamma} = -\boldsymbol{n}_{f,\Gamma} \tag{2.21}$$

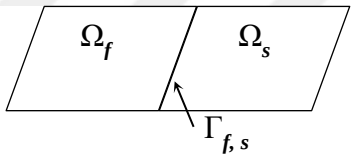

Figure 2.1 : Flow and structure domains seperated by a wet-surface.

2.3.2 Description of flexible blood vessel

Considering the linear elastic material model for the deformation of the aneurysm wall, the constitutive equation can be defined using isotropic Hooke`s law,

$$\boldsymbol{\sigma} = 2\mu_s \boldsymbol{\varepsilon} + \lambda_s tr(\boldsymbol{\varepsilon}) \boldsymbol{I} \tag{2.22}$$

where λ_s is Lamé's first parameter, $\boldsymbol{I}$ is the unit tensor, $tr()$ denotes the trace of the matrix and $\boldsymbol{\varepsilon}$ denotes the classical Cauchy strain tensor,

$$\boldsymbol{\varepsilon} = \frac{1}{2} [\boldsymbol{\nabla} \boldsymbol{D}_s + \boldsymbol{\nabla}^T \boldsymbol{D}_s] \tag{2.23}$$

$\boldsymbol{D}_s$ being the displacement vector in the solid part. The equation of motion for the linear elastic material hence can be written in terms of the local solid velocity vector $\boldsymbol{U}_s$ as,

$$\rho_s \frac{\partial \boldsymbol{U_s}^2}{\partial t^2}\,(\boldsymbol{\varepsilon}, t) \;-\; \boldsymbol{\nabla}\cdot[(2\mu_s + \lambda_s)\boldsymbol{\nabla D_s}] = \boldsymbol{\nabla}\cdot[-(\mu_s + \lambda_s)\boldsymbol{\nabla D_s} + \mu_s \boldsymbol{\nabla}^T \boldsymbol{D_s} + \lambda_s tr(\boldsymbol{\nabla D_s})\boldsymbol{I}] \quad (2.24)$$

2.3.3 Parameters of footprints of flow structures and solid motions

A wide variety of studies also showed that non-dimensional parameters based on the footprints of flow structures, particularly, the wall shear stress (WSS) in the aneurysm region can be exploited to reveal the characteristics of arterial flow and the complex wall response [44–46]. The time-averaged wall shear stress (TAWSS) is an integral value of the magnitude of WSS over a cardiac cycle

$$\text{TAWSS} = \frac{1}{T}\int_0^T |\text{WSS}| dt \quad (2.25)$$

and represents the tangential force on the surface of the arteries where high shear stress aligned in the direction of flow seems to promote endothelial cell survival [47]. Therefore, the TAWSS is one of the prevailing hemodynamic indexes used in blood rheology, but, as far as rupture risk assessment is concerned, the preference of either high or low TAWSS still remains controversial [48]. The oscillatory shear index (OSI) is a hemodynamic dimensionless metric that can help to characterize the flow as unidirectional or oscillating, and is a measure of the deviations of the wall shear stress vector from the direction of the mean flow throughout a cardiac cycle

$$OSI = 0.5\left(1 - \frac{\left|\int_0^T WSS dt\right|}{\int_0^T |WSS| dt}\right) \quad (2.26)$$

The OSI varies from zero to 0.5, in that zero OSI values show that the flow instabilities in the arteries are marginally small, while values near to 0.5 features strong deviations of the shear stress from the main flow direction [49]. Consequently, high OSI values indicate intimal thickening in the artery walls. Indeed, there is a large amount of statistical hemodynamic studies, which indicate that the coincidence of low TAWSS and high OSI in an arterial region appears to be the main indicator of rupture initiation [50,51].

The deformations in the wall of a cerebral aneurysm were also featured by its displacement which is directly linked with the von Mises stresses. The von Mises

stresses are therefore used to predict yielding or fracturing of materials under complex loading and can be written as,

$$\sigma_{von\ Mises} = \sqrt{0.5[(\sigma_{11} - \sigma_{22})^2 + (\sigma_{22} - \sigma_{33})^2 + (\sigma_{33} - \sigma_{11})^2 + 6({\sigma_{12}}^2 + {\sigma_{23}}^2 + {\sigma_{13}}^2)]} \quad (2.27)$$

where σ_{11}, σ_{22} and σ_{33} refer to normal stresses and σ_{12}, σ_{23} and σ_{13} correspond to shear stresses. In order to understand the correlation between material behavior and the hemodynamic stress analysis parameters (OSI and TAWSS), one then needs to compare the von Mises stress distribution with those of the OSI and TAWSS.

3. NUMERICAL IMPLEMENTATIONS

3.1 Patient-Specific Aneurysm Geometries and Flow Domain

Two patient-specific cerebral aneurysms studied in the present investigation. The first patient (Figure 3.1a) was a female of 41 years old, who had anterior communicating artery aneurysm with concomitant subarachnoid hemorrhage and left frontobasal hematoma. At angiography, an irregularly circumscribed aneurysm was detected in the anterior communicating artery, including the right A1-A2 junction, with a slightly anterior-downward oriented bilobed shaped of approximately 6.5×4.5×3.5 mm in size.

The second patient (Figure 3.1b) was a female of 62 years old, who had dolichoectatic carotid and vertebral arteries. A complex aneurysm with a bilobed contour of size of 13×8 mm was detected in the roof of the cavernous segment of the right internal carotid artery. No additional pathological features were detected in intracranial arterial segments and parenchymal venousphases were natural. The 3D images in digital imaging and communications in medicine format were anatomically remodeled into patient-specific 3D geometries in the STL format.

Both aneurysm cases consisted of three boundary patches: the inlet, rigid walls and outlets. During the finite volume mesh generation process, tetra elements were formed within the core region, connected with 3 layers of prism elements in the vicinity of the walls. A further increase in the mesh resolution was achieved in regions of critical importance, and the overall mesh consisted of roughly 300,000 cells (Figure 3.1).

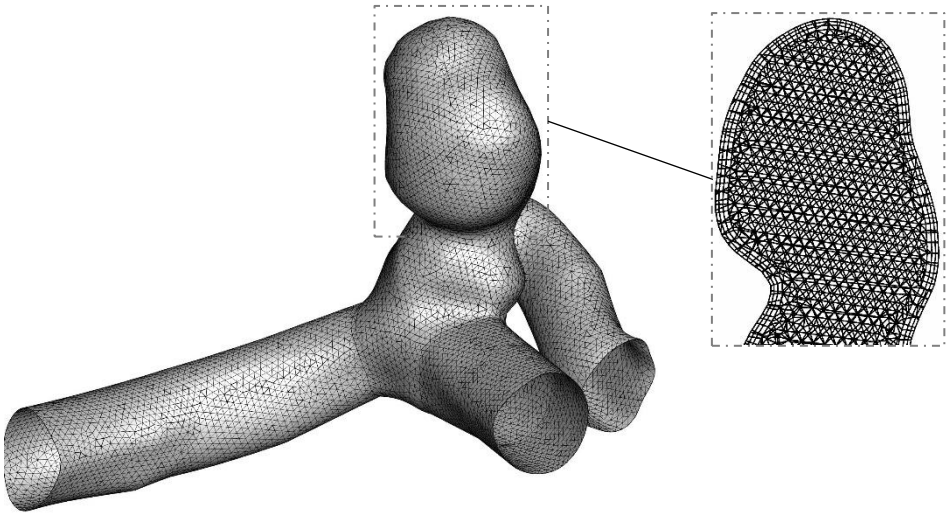

a) Patient-1

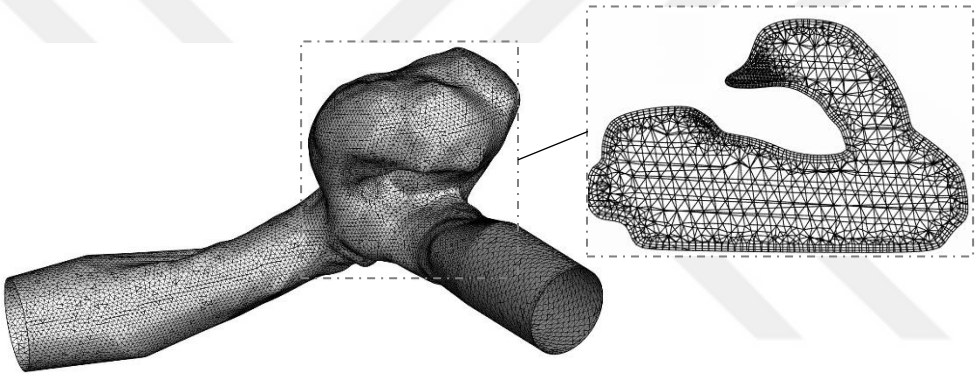

b) Patient-2

Figure 3.1 : Patient-specific aneurysm models and the corresponding 3D meshes.

3.2 Flow Solvers, Boundary Conditions and Numerical Schemes

For the CFD analysis the OpenFOAM software is used as the computational platform. Since there are two sets of Navier-Stokes equations, one needs to specify velocity and phase volume fractions for both phases separately. The time-varying velocity, corresponding to the two inflow pulses between systole and diastole (Figure 3.2) measured in the internal carotid by Ford et al [52] was used as the inlet boundary condition., no-slip at the walls and a Neumann-type boundary condition (pressureInletOutletVelocity) at the exit. The pressure field is represented in hydrostatic pressure, which was defined by a Neumann-type boundary condition (fixedFluxPressure) at the inlet and at the walls and, at the exit, a Dirichlet-type

boundary condition (prghPressure) prescribed by an atmospheric value of 101325 Pa is applied. The phase fractions are described by a Neumann-type boundary condition (zeroGradient) at all boundaries except for the inlet, where they were defined by a Dirichlet-type boundary condition. The discretization schemes used are; for the gradient, Least-Squares Gauss linear, for the divergence Gauss vanLeer, for the convective fluxes Gauss linear upwind and finally for the Laplacian term Gauss linear corrected. A first-order Euler formulation is used as the time scheme. The CFL (Courant Friedrichs Lewy) number is fixed at 0.5 so that an adjustable time stepping from 10^{-6} to 10^{-5} s is used. The PIMPLE algorithm, which, as far as the efficiency is concerned, has the advantages of both the SIMPLE (Semi-Implicit Method for Pressure-Linked Equations) and the PISO (Pressure Implicit with Splitting of Operator) algorithms and, therefore, is used with 3 outer corrector loops. The strategy is to implement iteratively the Flux Corrected Transport technique using the MULES (Multidimensional Universal Limiter for Explicit Solution) algorithm to ensure the boundedness in the solution of hyperbolic problem. 28 processors were utilized for the computations run with an accuracy (residual) of 10^{-6}.

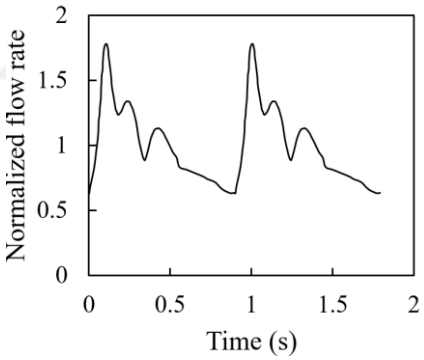

Figure 3.2 : Measured normalized flow rate for the internal carotid [52].

3.3 Structural Solvers, Boundary Conditions and Numerical Schemes

Considering the FSI analysis, the patient-specific cerebral aneurysm geometry studied in the present investigation was exactly the same as patient-1 (The patient was a female of 41 years old, who had an anterior communicating artery aneurysm with concomitant subarachnoid hemorrhage and left frontonasal hematoma). Here, the vessel wall structure was also augmented as well (Figure 3.3). The 3D mesh of the solid domain is consisted of roughly 12000 elements.

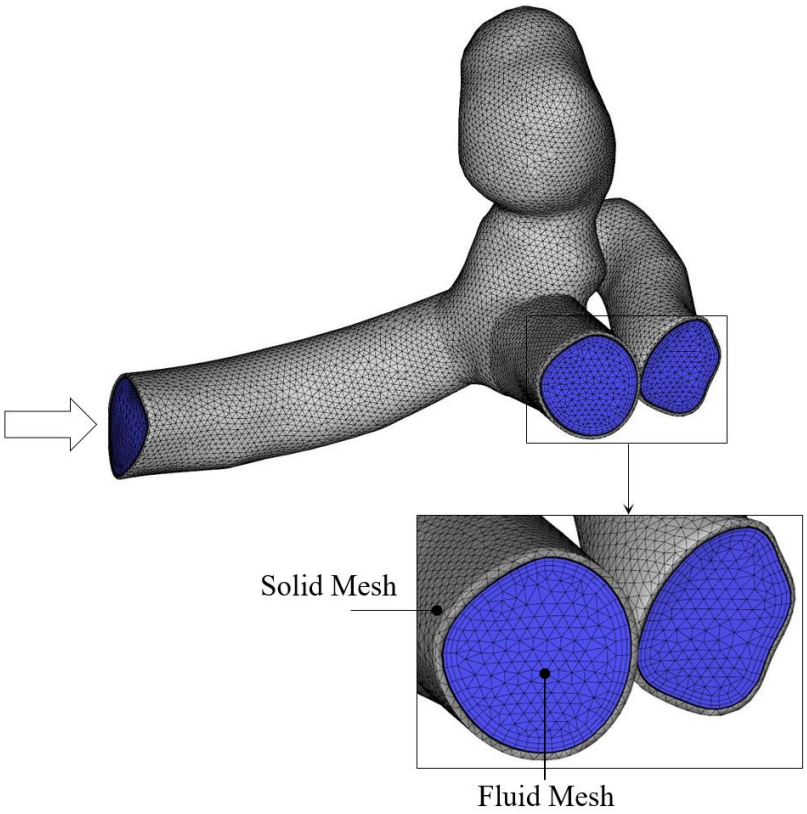

Figure 3.3 : Patient aneurysm model and the corresponding 3D meshes used in FSI.

For the structural analysis, the CALCULIX finite element (FEM) solver [53] was used where the Young's Modulus and the Poisson ratio in the linear elastic model were set as 1 MPa and 0.49, respectively. Furthermore, among three boundary patches the

deformable walls were set free to move in all directions, but the ends (the inlet and outlets) were completely fixed.

An open-source code, the preCICE, was used as the coupling tool (Figure 3.4), which offers two coupling schemes (explicit and implicit) for the execution order of the finite volume CFD and finite element structural solvers. The explicit (weak) scheme couples the fluid and solid participants once per time window, which does not have sufficient complexity for the current analysis. The implicit (strong) scheme, however, uses the FSI coupling convergence criteria in the multiple times until the convergence is achieved, and is more suitable for frequent and complex structural deformations [31,37].

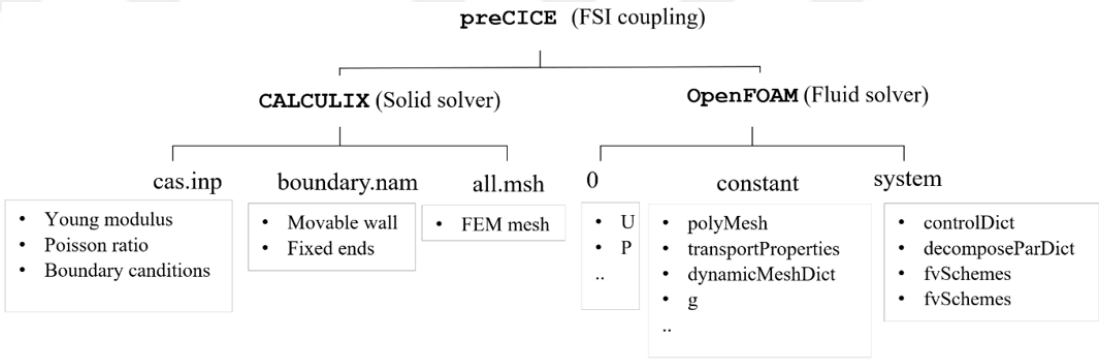

Figure 3.4 : FSI directory structure in the preCICE used for analysis of aneurysm.

4. CFD ANALYSES OF SINGLE- AND TWO-PHASE BLOOD FLOWS IN ANEURYSMS AND THEIR USE IN IDENTIFYING THROMBOSIS FORMATION AND RISK ASSESSMENT

In this chapter, the blood transport has been investigated using the single- and the two-phase methods. In two-phase Euler-Euler approach, the blood is represented by two interpenetrating continua where the dispersed red blood cells of non-Newtonian characteristics are suspended in the continuous Newtonian plasma. The results of two-phase model, where the RBCs phase is assumed to be Carreau–Yasuda fluid, are validated against the experimental data. Furthermore, comparative analyses were performed in two patient-specific aneurysms, which indicated that for a given pulsatile flow rate, the two-phase blood approach has vitally advantageous over the single-phase assumption, and revealed a deeper inflow penetration, more complex flow structures and denser flow diversion zones in the aneurysm sac. It was obvious that the high OSI values calculated by the two-phase model covered much wider regions than the single-phase predicted. It was equally crucial that these regions coincided with the TAWSS values lower than the threshold that the single-phase approach can predict. Apparently, the single-phase model failed to spot sites of high rupture risk. The results were further exploited to identify the RBCs aggregation regions as, for example, the concave structures and narrow paths in the saccular aneurysms, for their possible use as the precursors of the thrombus formation.

4.1 Two-Phase Model Validation Against the Experimental Data

The experimental configuration by Karino and Goldsmith [54] presents a perfect flow case to observe the advantages of the two-phase model results and attracts a considerable attention in the development of computational models because of its well-defined boundary conditions.

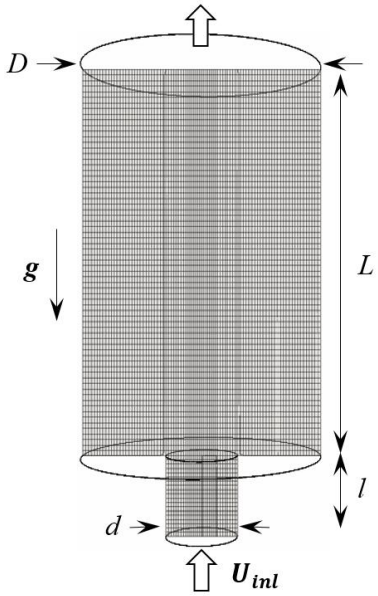

Figure 4.1 : Flow configuration [54] and meshing of the computational domain.

The computational setup is designed to match the experiment, Figure 4.1, which was comprised of a large glass tube with a length of L = 700 μm and diameter D = 504 μm and a cylindrical inlet with a length of l = 150 μm and diameter d = 154 μm. The flow with uniform velocity, U_{inl}, enters through the inlet cylinder, expands into the large tube and exits from the top. In two different cases, the inlet velocity is set to 0.0757 ms^{-1} and 0.233 ms^{-1}. Fluid properties and hematocrit values are given in Table 4.1.

Table 4.1 : Parameters used in the numerical setup for 1% hardened human red cells.

Parameter	Value
RBCs density	1100 kg m^{-3}
Plasma density	1060 kg m^{-3}
RBCs diameter	7.2 μm

For the validation simulations, the balance equations described in Section 2 are solved by a finite-volume method on a mesh of hexahedral volume elements in multi-block structured topology, which allows grids of high resolution. The computational domain was discretized in a 3D grid of 170,000 cells (see Figure 3.2) and the OpenFOAM software [55] is used as the computational platform. The velocity at the inlet was described by a Dirichlet-type boundary condition [56] with a uniform value (in the OpenFOAM terminology, it is referred as fixedValue), no-slip at the walls and a Neumann-type boundary condition (pressureInletOutletVelocity) at the exit. The pressure field is represented in hydrostatic pressure, which was defined by a Neumann-

type boundary condition (fixedFluxPressure) at the inlet and at the walls and, at the exit, a Dirichlet-type boundary condition (prghPressure) prescribed by an atmospheric value of 101325 Pa is applied. The phase fractions are described by a Neumann-type boundary condition (zeroGradient) at all boundaries except for the inlet, where they were defined by a Dirichlet-type boundary condition. The discretization schemes used are; for the gradient, Least-Squares Gauss linear, for the divergence Gauss vanLeer, for the convective fluxes Gauss linear upwind and finally for the Laplacian term Gauss linear corrected. A first-order Euler formulation is used as the time scheme. The CFL (Courant Friedrichs Lewy) number is fixed at 0.5 so that an adjustable time stepping from 10^{-6} to 10^{-5} s is used. Ten processors were utilized for the computations run with an accuracy (residual) of 10^{-6}. Figure 4.2 provides the contours and streamlines of the RBCs velocity field for the two inflow velocities (U_{inl} = 0.0757 ms^{-1} and 0.233 ms^{-1}). The most important feature of the flow is the toroidal vortex, which is perceived as two symmetric vortices on the sampling plane presented. The inflow penetrates through this vortex into the large tube and, after the reattachment point, the fully developed flow moves towards the exit. It is apparent that the vortex becomes stronger and larger with the momentum of the inflow. However, inside the toroidal vortex, there always exists a low velocity region, which is critical for the RBCs aggregations. Thus, the small vortex structure (Figure 4.2a) creates a less dynamic and stable zone for the RBCs aggregation compared to the large vortex (Figure 4.2b) where the velocities are much larger. The velocities probed along the line AB (in red color) crossing through the center of the vortex is expected to provide useful data for studying the rheological features of the RBCs. It is apparent that in both cases (U_{inl} = 0.0757 ms^{-1} and 0.233 ms^{-1}), the numerical simulations show an excellent agreement with the measurements. Hence, it is concluded that the two-phase flow approach and the Carreau–Yasuda viscosity model both have a great potential to predict the blood flow with proper consideration of the plasma and the RBCs.

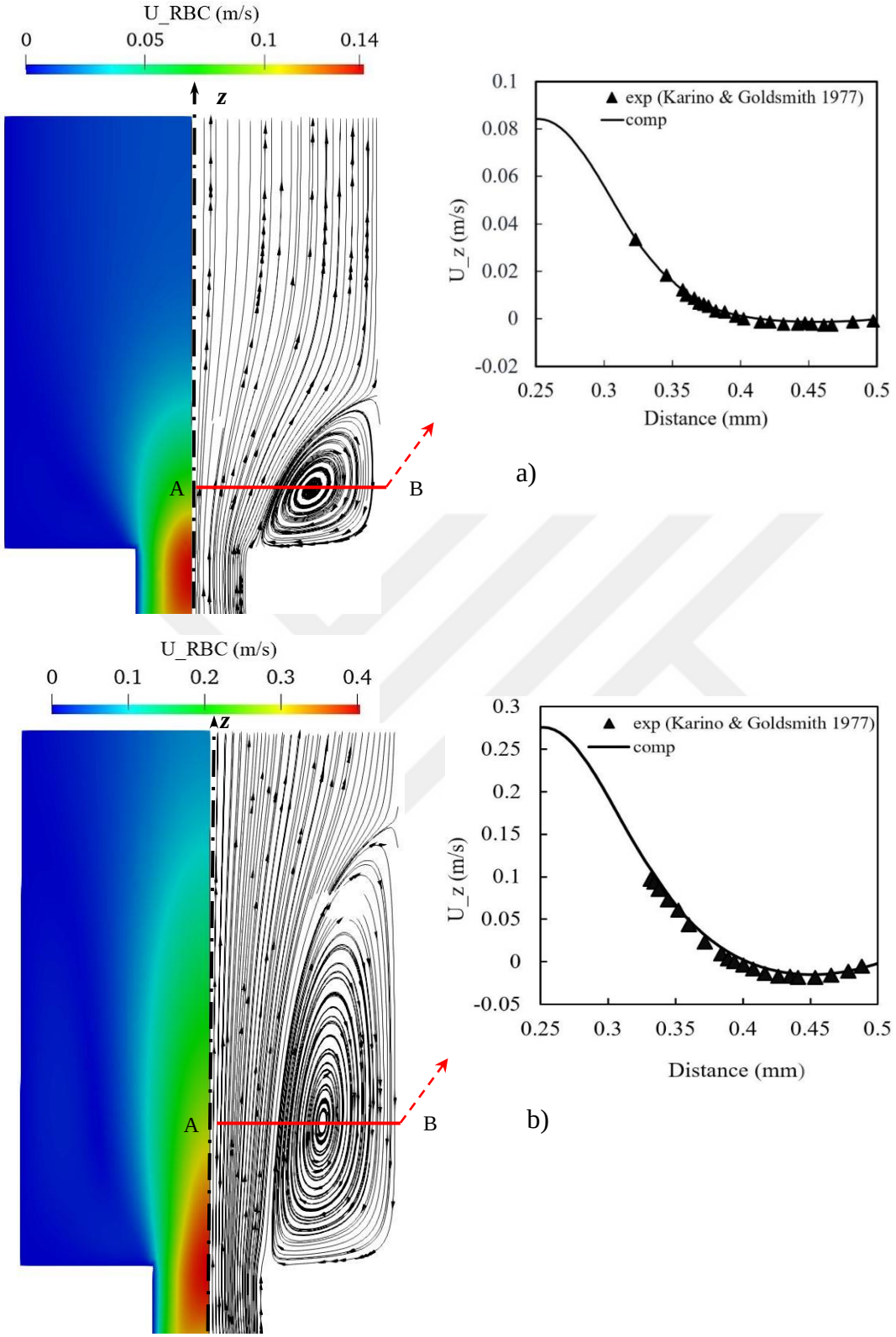

Figure 4.2 : Velocity of the RBCs: a) U_{inl} = 0.0757 ms^{-1} and b) U_{inl} = 0.233 ms^{-1}.

4.2 Application to Aneurysm Cases

4.2.1 Inflow concentration depth

Figure 4.3 shows the inflow jet concentrations for the single- and two-phase configurations. An examination of the velocity contours reveals that the inflow features observed in the single-phase flow computation remain relatively simple and stable, lacking the sufficient information about the inflow pattern inside the aneurysm sac. The two-phase blood model, on the other hand, presents significantly deeper penetrations with complex and unstable flow structures. It is obvious that while the single-phase model fails to identify the imminent threat to the patients' life, the two-phase model successfully captures the risky flow penetrations into the aneurysm sac. When we assess the rupture risks of both patients by considering the two-phase model predictions only, it is apparent that compared to the Patient-1, the penetration seems much deeper in the Patient-2, forming a helical open loop inside the aneurysms dome. We anticipate that the circulating flow in the helical loop will be more prone to generate higher order flow modes and, thus, acts as a continuous source of instability. This condition eventually leads to fluctuations at various time and length scales, each of which makes its own contribution to degrade the structural integrity of the aneurysm wall.

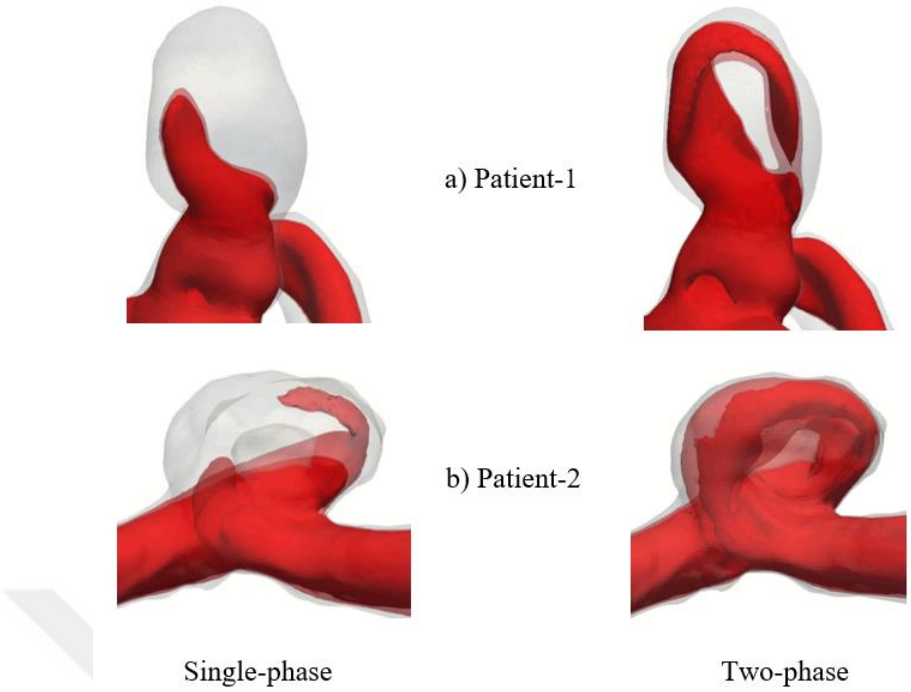

Figure 4.3 : Inflow concentration depth at the peak systole.

4.2.2 Flow complexity

The complexity of flow is another hemodynamic measure, where the CFD simulations make a significant contribution to the risk assessment. Figure 4.4 presents the characteristics of the blood flow at different sections normal to the aneurysm sac. It is beyond doubt that the two-phase blood model was considerably better to unveil the details of the flow within the ballooned region, in that the vortex structures appear larger in number and in strength than in the single-phase flow model. We know that the presence of such complex structures inside the aneurysm is the major cause of the aneurysm rupture. Particularly, the blood flow of the Patient-2, where a toroidal vortex structure existed inside the aneurysm dome, is more involved with the formation of the secondary vortices, which prove the previous assertion on the higher order modes. Furthermore, the lower velocities predicted by the single-phase model indicate longer residence times, which result in incorrect perceptions as if less fluctuations occurring in the wall shear stress and its direction. This, of course, falsely reduces the true rupture risk in high-risk cases.

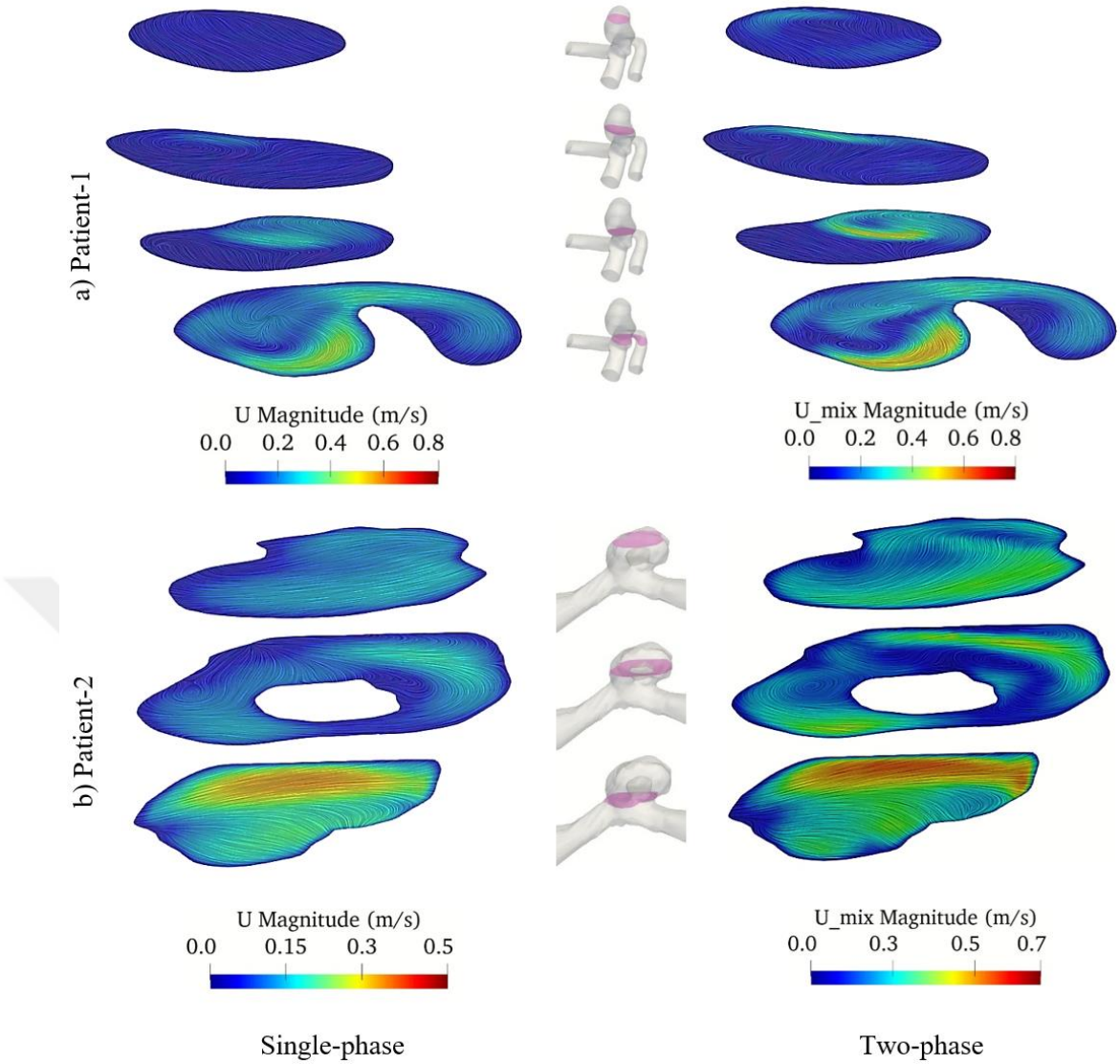

Figure 4.4 : Velocities and streamlines in the aneurysm's sac at the peak systole.

4.2.3 Flow impingement zone

Except for the slightly lower velocities observed in the single-phase calculations, Figure 4.5 shows that both flow models work surprisingly well in predicting the diversion of the inflow by the walls in the aneurysm region. The results, however, reveal that the inflow in the aneurysm region of the Patient-1 (Figure 4.5a) impinges with a very high momentum on an area as large as half the aneurysm region. These conditions seem to elevate the wall shear stress and develop undulations on the surface, which concurrently results in rapid changes in the direction of the wall shear stress. This situation remarkably increases the rupture risk for the Patient-1 compared to the

Patient-2. Evidently, even this piece of information plays a vital role in the assessment of aneurysm statues.

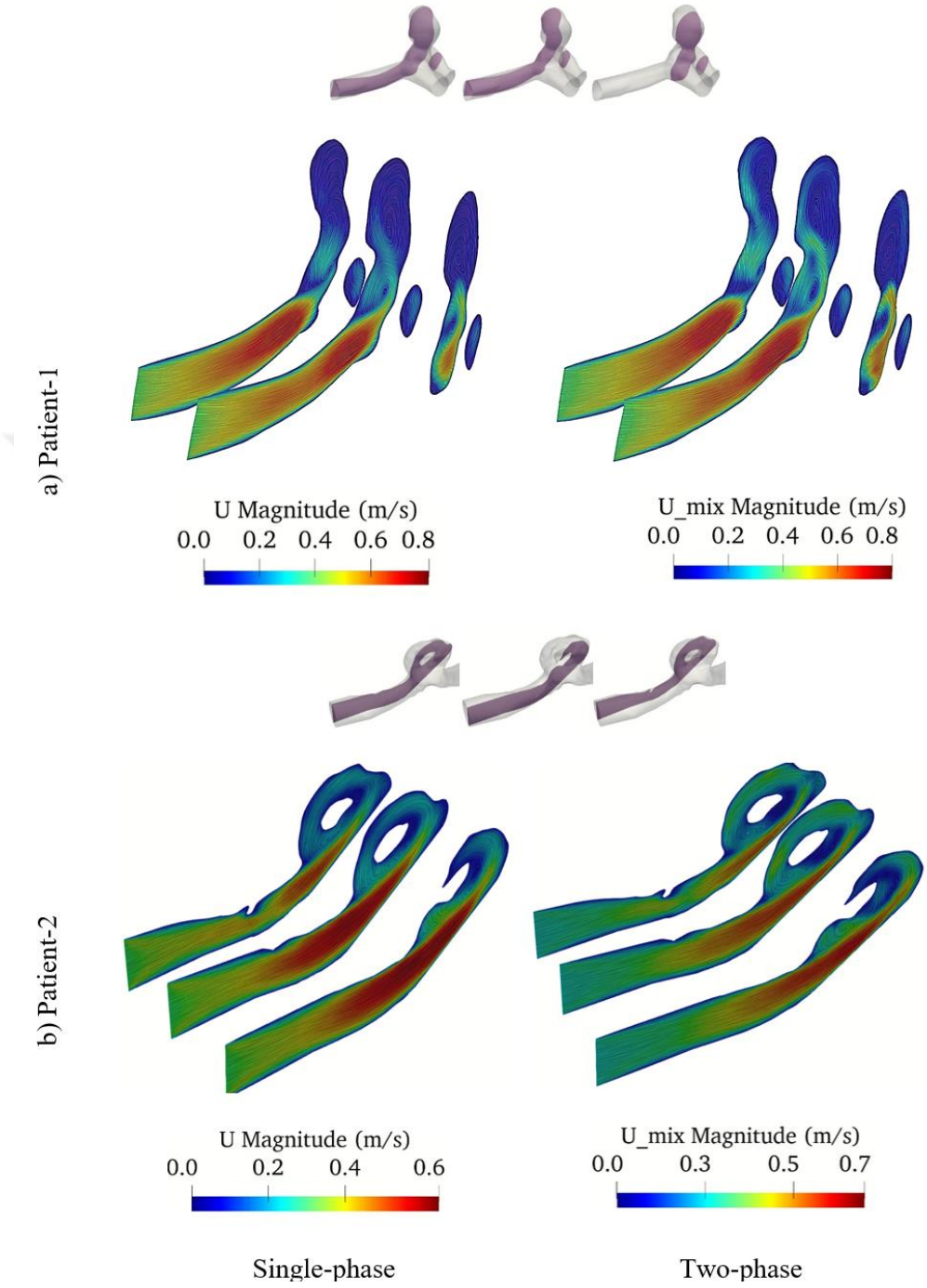

Figure 4.5 : Details of flow in the impingement zone at the peak systole.

4.2.4 Velocity profiles

The velocity profiles over L1, L2 and L3 cross lines passing through the aneurysms sac region were extracted for the single- and two-phase configurations (Figure 4.6).

These locations were selected because the primary inflow stream ends its way in the aneurysm sac before rejoining the upcoming stream, where the flow field becomes more complex as the upcoming flow encounters with a stronger primary stream. Thus, it can be said that as the primary flow field preserve its momentum throughout the aneurysm sac, the risk of rupture would be increased simultaneously. It is clear that for both aneurysms, the two-phase flow shows significantly higher (1.5 times higher) velocity values. Also, it has been known that the depending on characteristics of the inflow jet, a secondary sac formation develops inside the aneurysm region. Hence, the shape and the values of velocity profiles becomes critically important to determine the growth direction of the aneurysms and a possible formation of a daughter sac. The two-phase results demonstrate two companion velocity peaks at the L1 and L2 locations, which merge into a single peak at the L3. It should be emphasized that the sharpness of the peaks makes them even more critical for a possible surface deformation in the aneurysms sac. The single-phase results, on the other hand, exhibit relatively milder velocity gradients with no severe peak inside the sac, though the sac region contains several surface inflations large enough to divert the flow field.

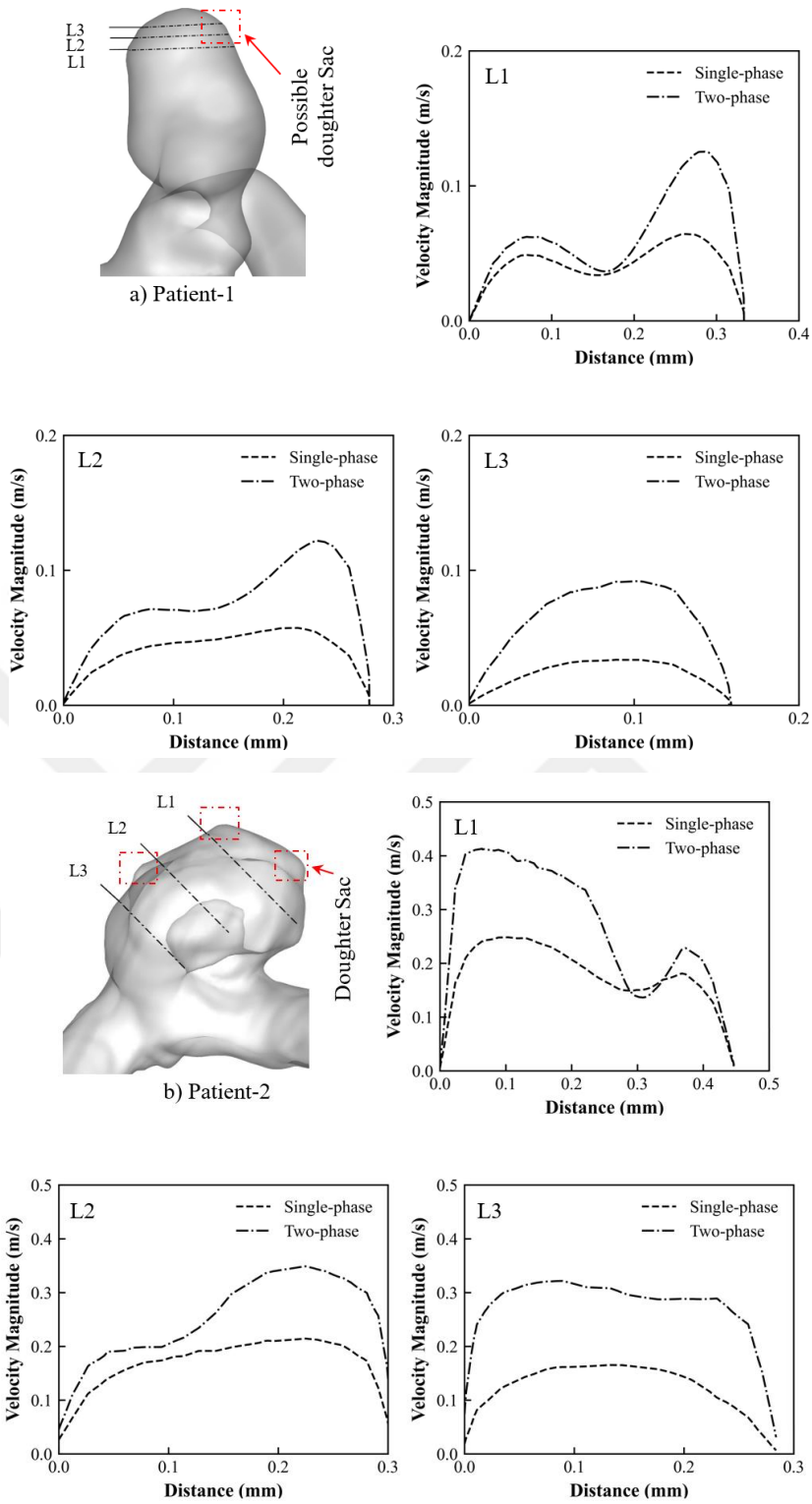

Figure 4.6 : Velocity profiles within the aneurysm sac regions at the peak systole.

4.2.5 Wall shear stress based hemodynamic analysis

As we have mentioned in section 2.4, the wall shear stress (WSS) based hemodynamic analysis is a prevailing assessment tool in the aneurysm initiation, growth and rupture where the high WSS is associated with the initiation phase and the low WSS is

supposed to contribute to growth and rapture phases. In the present investigation, the clinical reports provided for the both patients indicate that the size of the aneurysms is large enough to consider a rupture risk. Hence, we need to consider a combination of WSS based indexes such as OSI and TAWSS values. But before discussing the time-averaged values, we will first consider the instantaneous WSS values at different spatial locations for the single- and two-phase calculations. Figure 4.7 shows that the maximum instantaneous WSS occurs near the aneurysm neck region, whereas the lower values are observed in the tip and bleb regions. The WSS values calculated for the single-phase model are seen to be higher than the WSS values for the two-phase model at points P1, P2 and P3 of the Patient-1 and the point P1 of the Patient-2. As we moved from the higher flow region (neck zone) toward the lower flow region (tip and bleb zones), the two-phase model gives higher WSS values than those of the single-phase model. A close examination of the WSS values of the two-phase model at different locations also shows that the values of hemodynamic forces are predominantly determined by the values of the RBCs and this becomes even more apparent if the hematocrit rate is above the normal rate (%45). And this is an important feature, which is not possible to observe in a single-phase calculation. Comparing the measures of the shear stress, TAWSS and OSI, for both single- and two-phase calculations, Figure 4.8, it was evident that the results were not coherent in terms of magnitudes and locations of the extreme values. The single-phase approach predicted the TAWSS values by roughly 50% higher for both aneurysm cases. Besides, at locations with low TAWSS values, the single-phase indicated a very small area where large OSI values were prevailing. Since the coincidence of minimum TAWSS and maximum OSI values are of major concern, the single-phase model therefore exhibits a much lower risk factor compared to the two-phase model. This once again confirms the inadequacy of the single-phase model to capture the true risk. A much robust performance of the two-phase approach in the risk assessment can be attributed to its capability of representing the non-Newtonian RBCs suspended in Newtonian plasma, which produces useful information on the RBCs aggregations. Hence, a further examination of two-phase results reveals that the Patient-2 (Figure 4.8b) have multiple regions, where the minimum TAWSS and the maximum OSI values were coincident, and, thus, carries more rupture risk than the Patient-1 (Figure 4.8a).

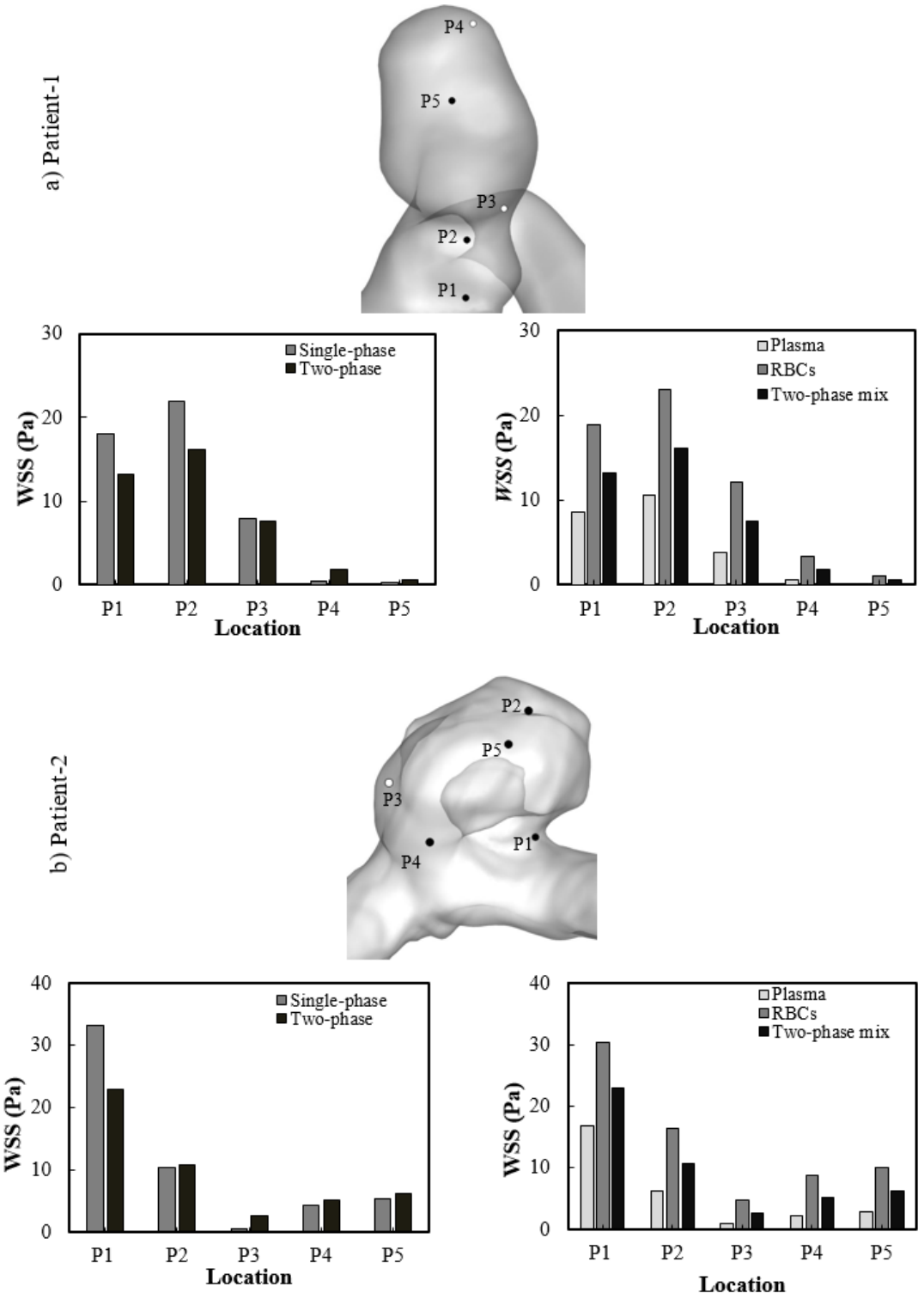

Figure 4.7 : Local variation of WSS on the aneurysm sac at the peak systole.

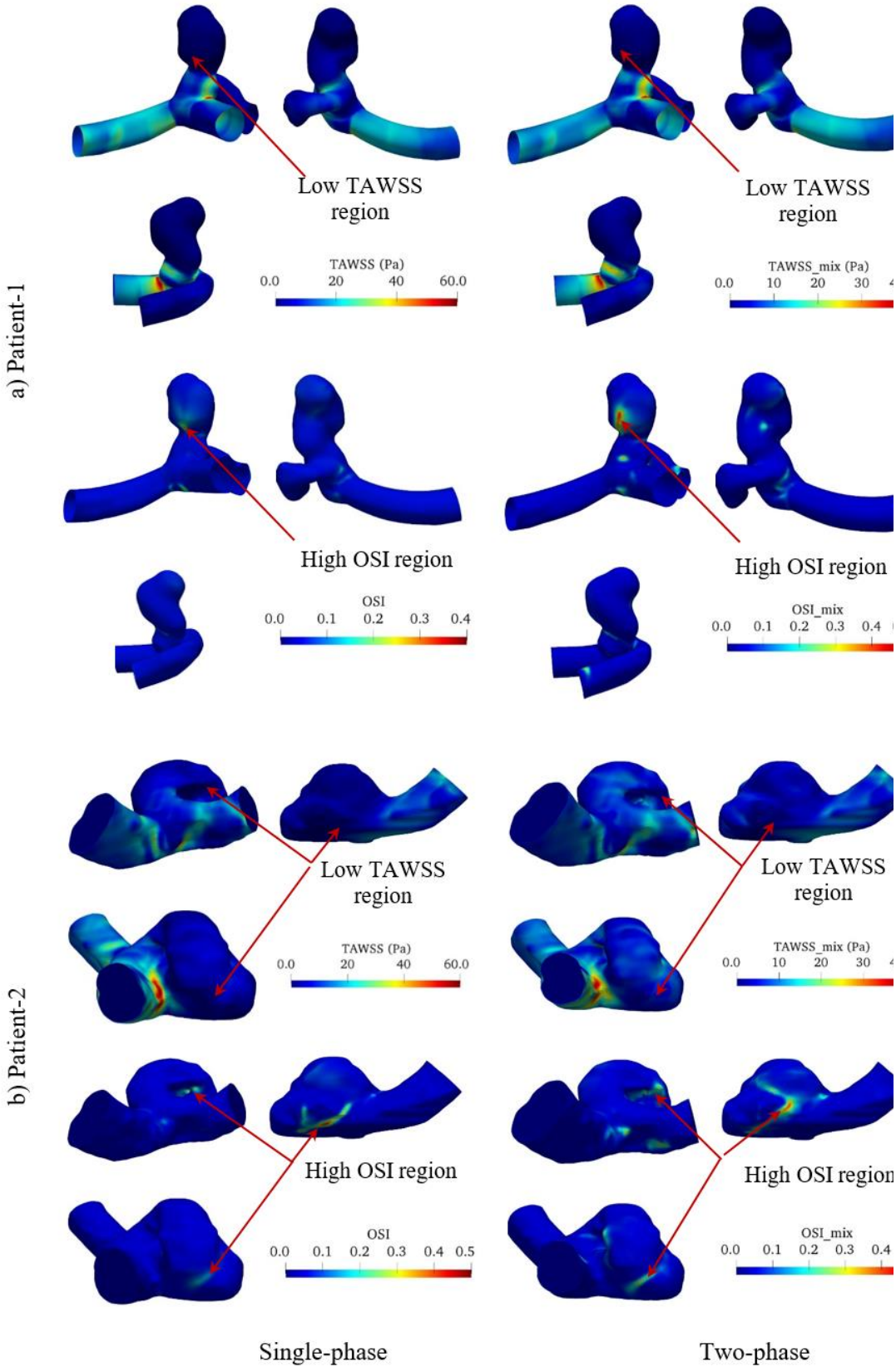

Figure 4.8 : Coincidence of low TAWSS and high OSI regions.

4.2.6 Possible regions of thrombus formation

Since the two-phase approach solves an independent set of equations for the RBCs, we believe that we can quantitatively search and analyze the possible regions of thrombus formation in our patients. It should be noted that both patients under consideration have small size aneurysms and, thus, the thrombus formation may not occur except in the regions containing concave surfaces or narrow passages. In order to identify potentially critical regions where the aggregation likely to occur, the phase fraction of the RBCs was averaged over one cardiac cycle for the Patient-1 on a concave shell (Figure 4.9a) and for the Patient-2 in a restricted pathway (Figure 4.9b). The Patient-1 and the Patient-2 both seem to have aggregations with RBCs concentrations exceeding the input value of 0.45 by up to 0.9% and 1.3%, respectively. Since the formation of thrombosis in the Patient-2 occurs at the constriction of the aneurysm sac, the wall degradation in this patient is expected to be more critical.

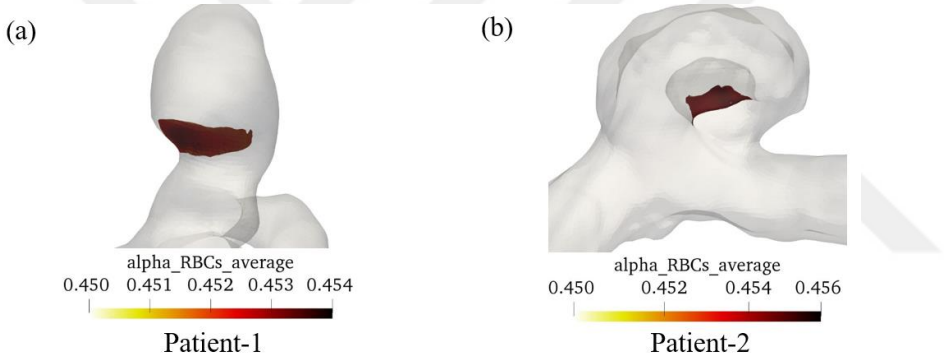

Figure 4.9 : Potential zones for RBCs aggregation in concave and narrow paths.

5. AN APPLICATION OF TWO-PHASE BLOOD FLOW IN PATIENT-SPECIFIC ANEURYSMS: EFFECT OF RBC CONCENTRATION

In this chapter, the effect of variations in the haematocrit level on the blood flow was studied in two cerebral aneurysms using the two-phase Euler-Euler approach and the Carreau–Yasuda viscosity model. The results showed that the maximum inflow jet penetration was achieved at the lowest haematocrit level, and this accompanied with strong flow impingements at the narrow corners deep inside the aneurysm sac and undesired complex flow patterns spreading from entrance to the aneurysm dome. The decrease in H level also changed the characteristics of the velocity profile inside the dome from a single- to a double-peak profile, which increased the likelihood of a daughter aneurysm formation. Furthermore, the TAWSS and OSI indicators showed that lowering the H values could change an initially low-risk case into a very high rupture risk situation.

The two-phase Euler-Euler approach was used to enlighten the effect of variations in the haematocrit level to cure the blood flow issue in two cerebral aneurysms. A comprehensive description of the two-phase Euler-Euler approach and the relevant viscosity specifications were described in the previous chapter. The same patient specific aneurysms and the numerical implementations of the two-phase model discussed before were used here. However, this chapter presents an appraisal of the approach and interpretations of the flow complexity, features of the inflow diversion zone, penetration depths and the shear stress parameters based on varying Hematocrit values.

5.1 Change in Inflow Jet Penetration Depth Based on Varying Hematocrit Values

We know that the penetration of inflow jet plays a major role in the aneurysm rupture [57]. Figure 5.1 shows the depth of the inflow jet for the hematocrit values ranging from H20 (extremely low) to H70 (extremely high) at the peak systole. It is clear that for both aneurysm cases, the maximum depths occur at the low end of the haematocrit values, where particularly H20, H25 and H30 present significantly deeper penetrations

with complex and unstable flow structures. The depth then gradually decreases as the H value increases. This is not surprising since increasing the blood mixture viscosity at low shear rates, the RBCs aggregation in the aneurysm sac prevents further penetration of the incoming flow. It should also be reminded that both extremely high and low H values suggest a weak oxygen supply capacity, leading to arterial wall weakening and so the vascular degenerative diseases.

When we consider the structural features of the flow penetration, we notice that the blood flow of the Patient-2 forms a helical open loop inside the aneurysms dome, and this indicates longer pathways or equivalently larger penetration depths, which deepens with the decreasing H values. It is not difficult to conjecture that the circulating flow will apparently be more prone to generate instabilities, which will cause fluctuations at various time and length scales to degrade the structural integrity of the aneurysm wall. Hence, when we assess the rupture risks of both patients, it is clear that compared to the Patient-1, the situation for the Patient-2 must cause most concern.

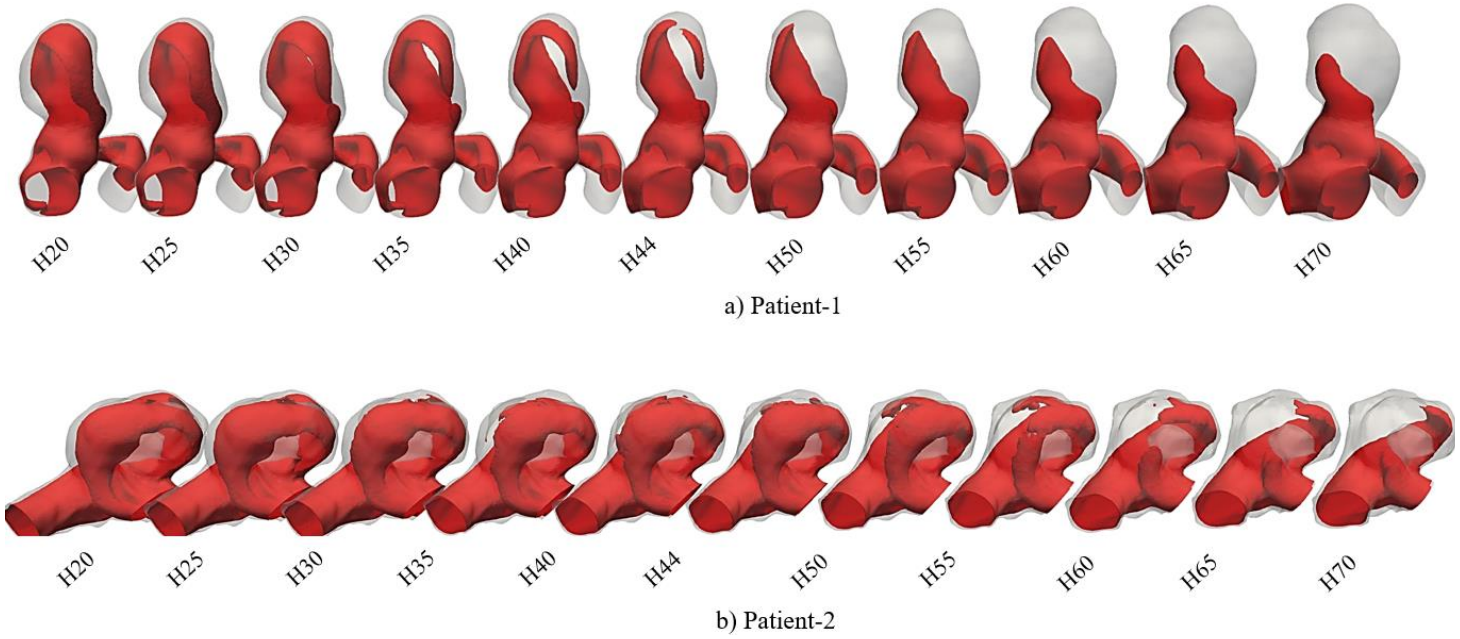

Figure 5.1 : Depth inflow jet penetration at the peak systole.

5.2 Change in the Streamlines Structure Based on Varying Hematocrit Values

We know that the presence of complex structures inside the aneurysm is the major cause of the aneurysm rupture, and if there exist multiple vortices in the sac region, the flow structure is considered as a complex pattern. Figure 5.2 represents the flow patterns at two cross-sections (in a region close to the neck and in the ballooned region) normal to the aneurysm sac for H values ranging from H20 to H70. Detailed examination reveals that the local flow complexity at different parts of the aneurysm dome is very dependent on the H value. For example, for the Patient-1, the flow for the high H values was complex both in the neck and in the ballooned regions. However, towards the lower end of the H values, particularly for H20, the complexity was shifted up and became mostly confined in the ballooned region. On the other hand, for the Patient-2, a trend slightly different than that for the Patient-1 was observed. For the higher H values, the complexity of the flow pattern was confined only in the neck region. However, as the H values decreases, the ballooned region became equally complex. Hence, it can be concluded that the reduction of the H values generates more complex flow structures in the aneurysm sac and promotes the risk of rupture in the cerebral aneurysms. The situation becomes even more serious for a complicated aneurysm geometry as, for example the Patient-2, where multiple zones in the aneurysm dome might present high risk of rupture.

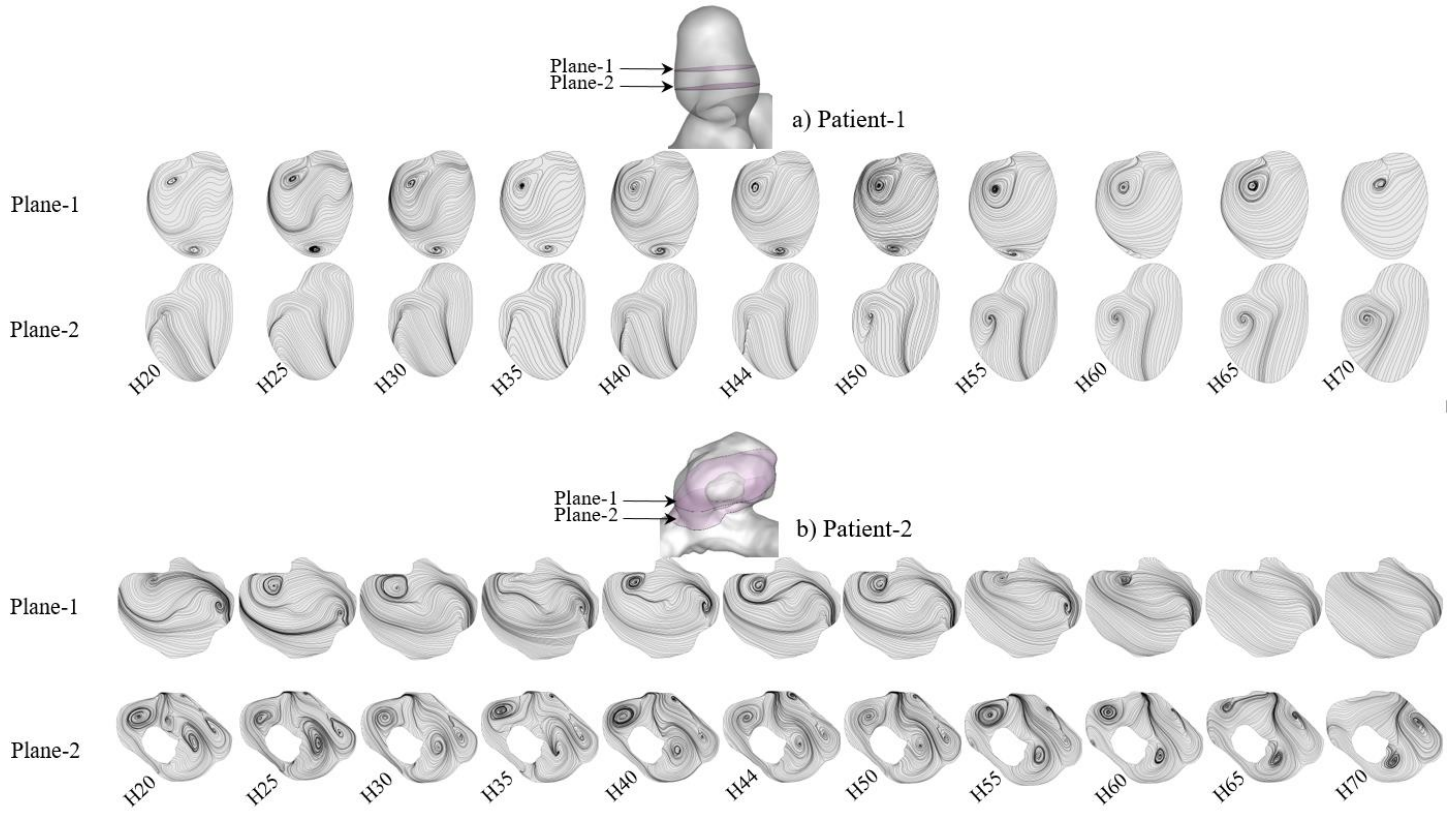

Figure 5.2 : Streamlines in aneurysms sac at the peak systole.

5.3 Change in the Flow in the Impingement Zone Based on Varying Hematocrit Values

The flow in the impingement zone is another deterministic factor in the field of aneurysm risk assessments. Figure 5.3 presents the velocity distributions in two aneurysm cases. It is clear that at the high H values, the penetration of the incoming flow is prohibited due to the accumulation of the RBCs in the aneurysm sac. Hence, the entrance length remains shorter, and this feature can at first glance be thought to decrease the risk of aneurysm rupture. However, as the H values decrease from H70 to H20, the inflow can reach the narrow corners located deep inside the aneurysm sac where the high-momentum inflow is forced to make a turn. Our results reveal that the diversion of the inflow jet after the impingement occurs milder for the Patient-1 compared to the Patient-2 where a much sharper turning takes place. The sharp turn in the toroidal structure of the aneurysm of the Patient-2 is expected to cause a larger momentum exchange with the wall and results in permanent deformations leading to contusion on the tissues. This agrees with the fact that if the area of impingement zone is small and if the velocity values are high in the cornering regions, the rapid change of the direction of the wall shear stress raises the risk of aneurysm rupture dramatically [12,58].

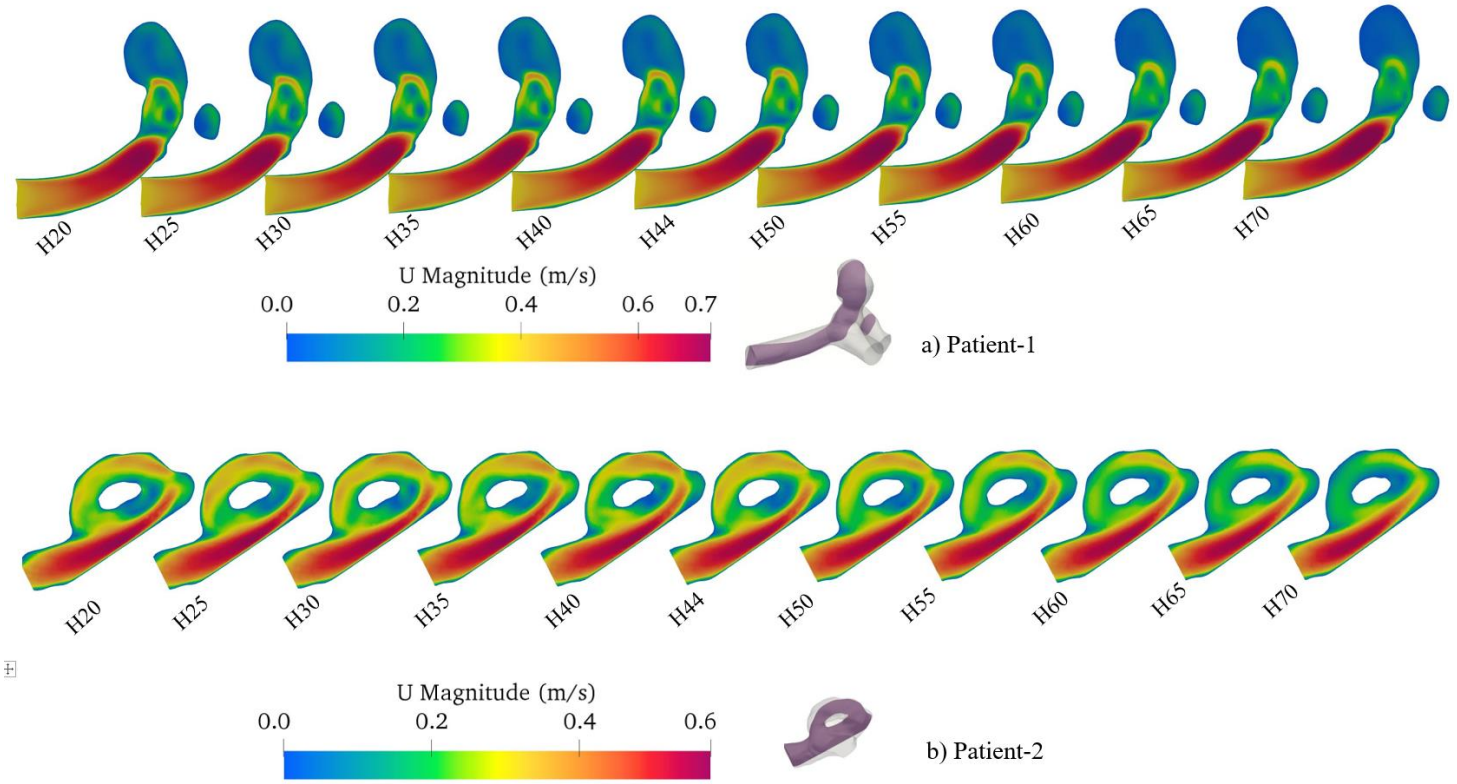

Figure 5.3 : Details of flow in the impingement zone at the peak systole.

5.4 The Change in Velocity Profiles Passing Through the Aneurysm's Sac Region Based on Varying Hematocrit Values

The flow in the impingement zone is another deterministic factor in the field of aneurysm risk assessments. In order to investigate the effect of blood composition on daughter aneurysm phenomenon, the velocity profiles over cross-lines (see Figure 5.4 for L1, L2 and L3) passing through the aneurysm's sac region were extracted for different H values from H20 to H70. It is clear that the same general features are observed for the both aneurysms, in that the velocity profiles obtained from the line L1 show two peaks whose magnitudes increase with the H values decreased from H70 to H20. The peaks gradually disappear on the velocity profiles obtained from the lines L2 and L3, which exhibit milder gradients, even though the lower H values demonstrate extremely higher velocity values. The high pressure attained at the wall proximity where the primary inflow was about to stop is expected to lead to a continuous deformation of the aneurysm walls in the direction perpendicular to the direction local momentum maximum. That is to say, if the magnitude of the shear at the vicinity of the wall becomes high, the risk of secondary (daughter) aneurysms will increase dramatically [59]. These results clearly show that the RBCs composition of the blood has strong influence on the pressure and wall shears stresses and, consequently, the risk of deformation and the formation of daughter aneurysms.

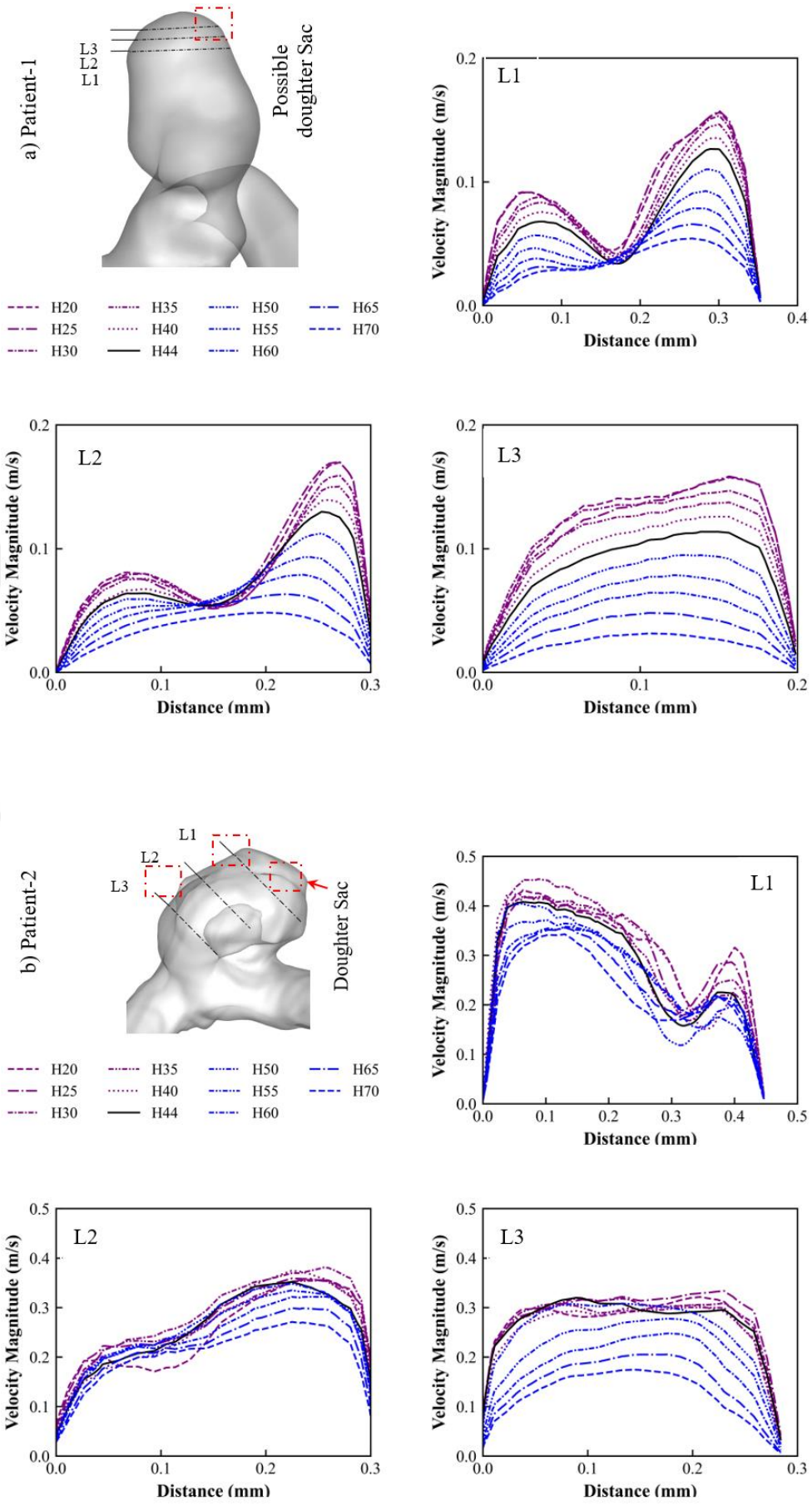

Figure 5.4 : Velocity profiles within the aneurysm sac regions at the peak systole.

5.5 The Change in Spatial Variations of the Instantaneous Wall Shear Stress (WSS*)* Based on Varying Hematocrit Values

The spatial variations of the instantaneous wall shear stress (WSS) are examined in Figure 5.5 for different H values ranging from H20 to H70. It is evident that for the both patients, the maximum values seem to occur near the neck region, where the RBCs' contribution to the WSS happens to be the largest particularly at the low end of the H range. Knowing the fact that the high shear stress aligned in the direction of flow seems to promote endothelial cell survival [47], the results indicate a decreasing probability of rapture in those regions. On the other hand, the lowest instantaneous WSS, which highlights the possible weakness, are observed in the tip and bleb regions: P4, P5, P6, P7 and P8 for the Patient-1 and P3, P4 and P5 for the Patient-2.

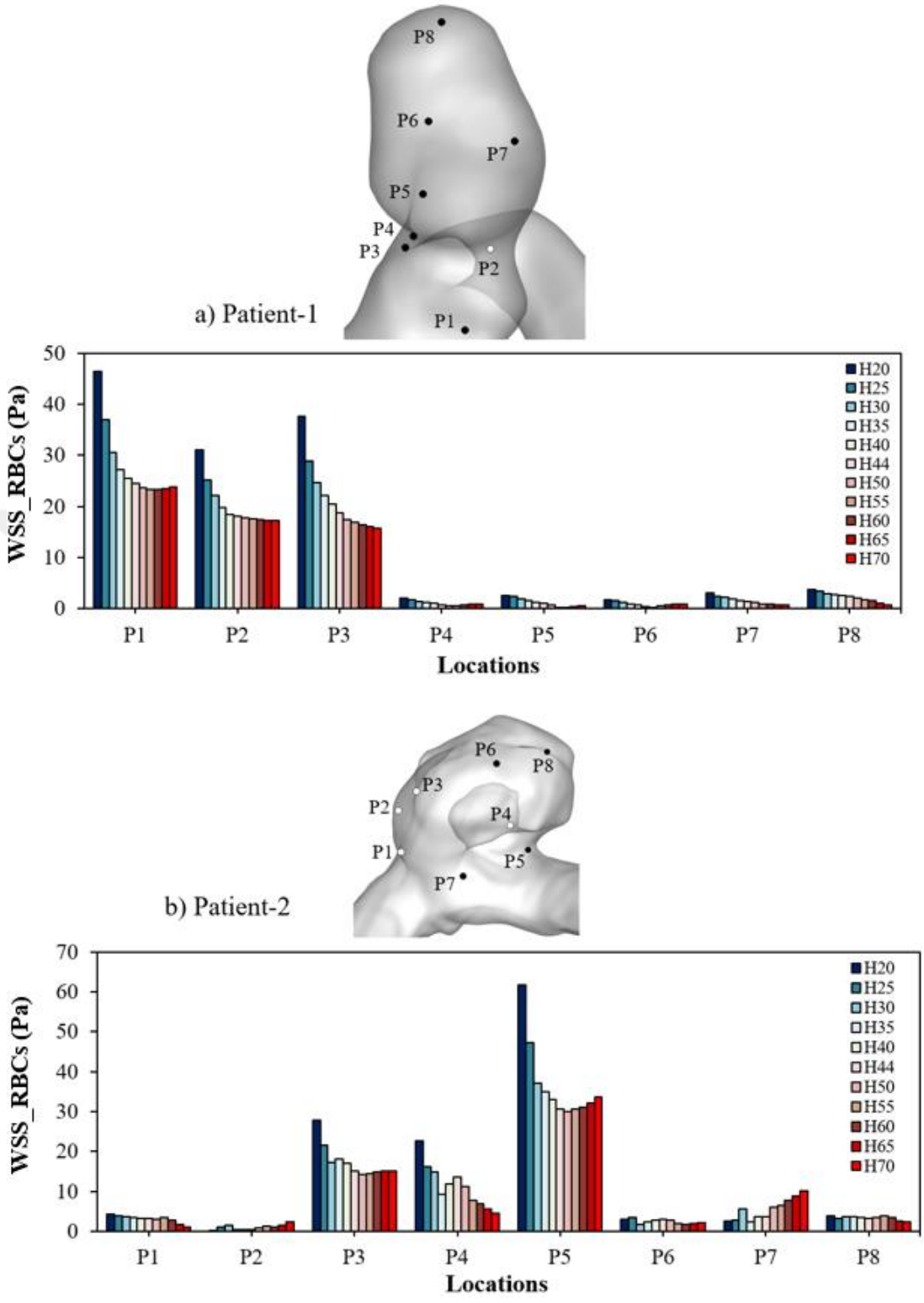

Figure 5.5 : Spatial variation of instantaneous WSS at the peak systole.

5.6 The Change in Spatial Variations of the Oscillatory Shear Index (OSI) and Time Averaged Wall Shear Stress (TAWSS) Based on Varying Hematocrit Values

The experiments have also revealed [60,61] that the magnitudes of the flow oscillations is also a measure of instabilities in the arteries. The deviations of the wall shear stress vector from the direction of the mean flow is represented by the oscillatory shear index (OSI) whose values can vary from zero (marginally small perturbations) to 0.5 (large perturbations) which indicate intimal thickening in the artery walls [49]. Indeed, there is a large amount of statistical hemodynamic studies [50], which suggest that the coincidence of high OSI and low time-averaged WSS values in an arterial region appears to be the main indicator of rupture initiation. Figure 5.6 shows the TAWSS and OSI values for different hematocrit levels. We first observe that the predicted TAWSS values for both patient specific aneurysms showed extremely low magnitudes around the sac region, where very large OSI values are observed. However, although this might be perceived as a positive finding, it must be emphasized that both the magnitudes and the locations of the extreme TAWSS and OSI were changing simultaneously with the H values. Considering the case of the Patient-1, the TAWSS values gradually decrease with the H values changing from H70 to H20. At the same time, there is also a gradual shift in high OSI regions from the entrance towards the middle sac. As a result, for the low hematocrit levels (< H35), the high OSI values exactly coincide with low TAWSS values. This shows that a large reduction in Hematocrit levels can change an initially low-risk case into a very high rupture risk situation. Yet the clinical reports have indicated that the middle face of the aneurysm sac for the Patient-1 becomes dangerously thin, which clearly demands an immediate attention.

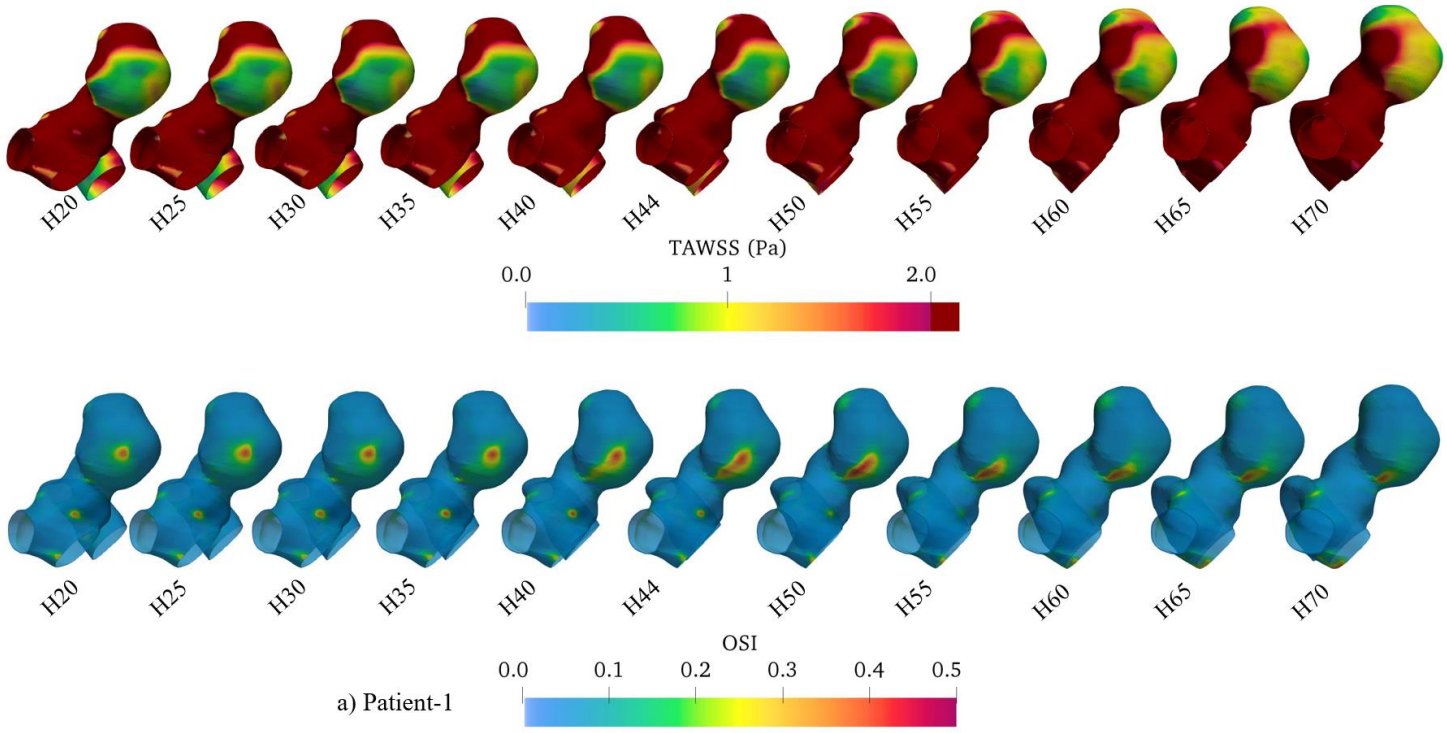
H20
H25
H30
H35
H40
H44
H50
H55
H60
H65
H70
TAWSS (Pa)
0.0
1
2.0
H20
H25
H30
H35
H40
H44
H50
H55
H60
H65
H70
OSI
0.0
0.1
0.2
0.3
0.4
0.5

a) Patient-1

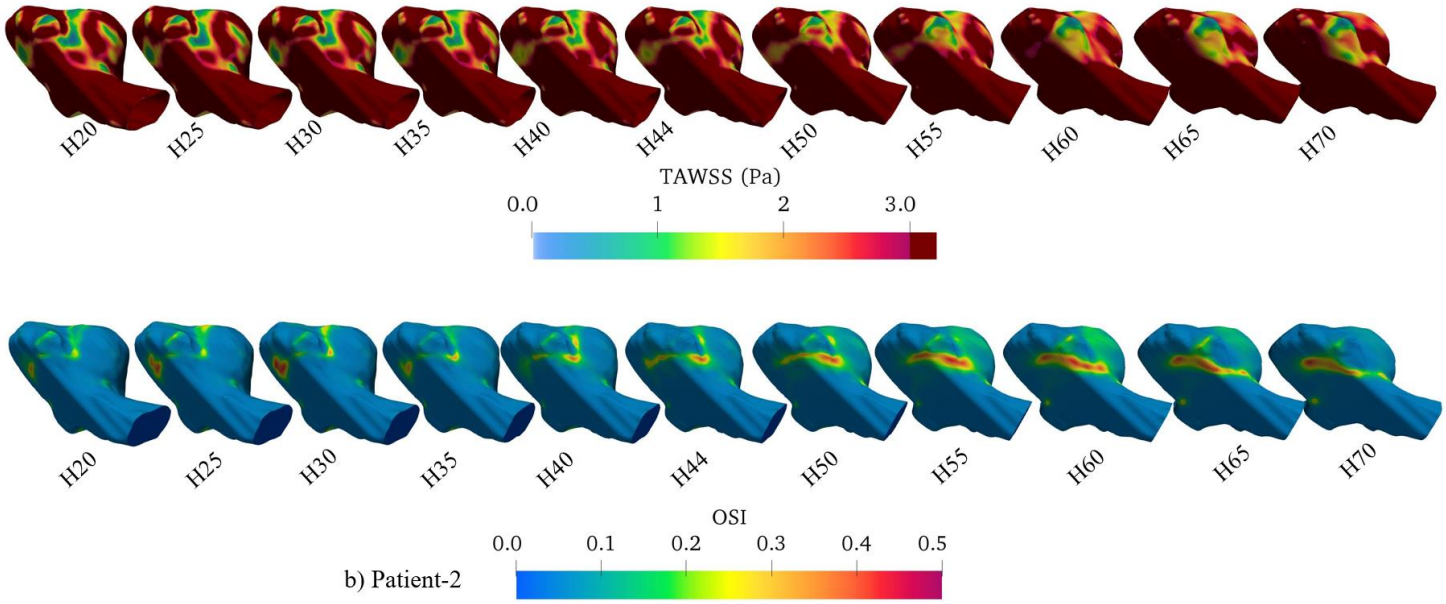

Figure 5.6 : Coincidence of low TAWSS and high OSI regions.

6. USE OF PARTITIONED FSI AND ALE METHOD FOR MODELING OF INTERACTIONS BETWEEN NON-NEWTONIAN BLOOD FLOW AND DEFORMABLE VESSEL

In this chapter, the dynamics of the wall movements of a patient-specific aneurysm dome were investigated using the interactions of the non-Newtonian blood flow and the deformable vessels. The patient under consideration had an anterior communicating artery aneurysm with a concomitant subarachnoid hemorrhage and left frontonasal hematoma. A finite volume CFD solver was used with a 3D mesh of roughly 300000 cells and three boundary patches; the inlet, deformable walls and outlets. A linear elastic material model was considered for the deformation of the aneurysm wall and, in the structural computations, a finite element solver was employed with a solid domain of approximately 12000 elements. An open-source code was exploited for the coupling between the CFD and finite element solvers. Results showed that at the peak systole, the vortical structure of the flow in the aneurysm dome was complicated. Furthermore, the instabilities in the flow field produced intense shear forces, due to which a possible weakening of the wall material will certainly lead to an increase in the risk of the rupture and bleeding. The non-uniformity of the flow field acquired large values of the von Mises stresses, resulting in prominent wall displacements, which also matched to the high OSI and low TAWSS values. The maximum displacements exhibited a non-stationery movement everywhere in the dome though mostly remained in the region of the impingement.

The governing equations describing the non-Newtonian viscosity model were discussed in previous chapters. Here, an appraisal of the FSI approach and its implementation, the governing equations regarding the single-phase blood assumption and mechanics of deformable vessel structure are discussed in detail.

6.1 Characteristics of Velocity Field

Earlier chapters have shown that the consistency of the flow field, particularly at the impingement zone, is one of the vital issues in the rupture risk assessment of cerebral

aneurysms. Figure 6.1 presents the magnitude of the flow velocity in the aneurysm dome, where the uniformity of the velocity field seems to degrade significantly in the flow impingement zone. In order to examine the changes in flow features due to the flow deflection over the turning, the velocity profiles on the cross-lines (L1, L2 and L3; see Figure 6.1) were probed. In the first profile (L1), the inertial forces upset the uniformity and pile up the flow on the outside the corner where a velocity peak is observed near the wall. Towards the L3, a location deep in the flow impingement zone, the velocity uniformity is recovered with an average value higher than that at the beginning of the impingement zone.

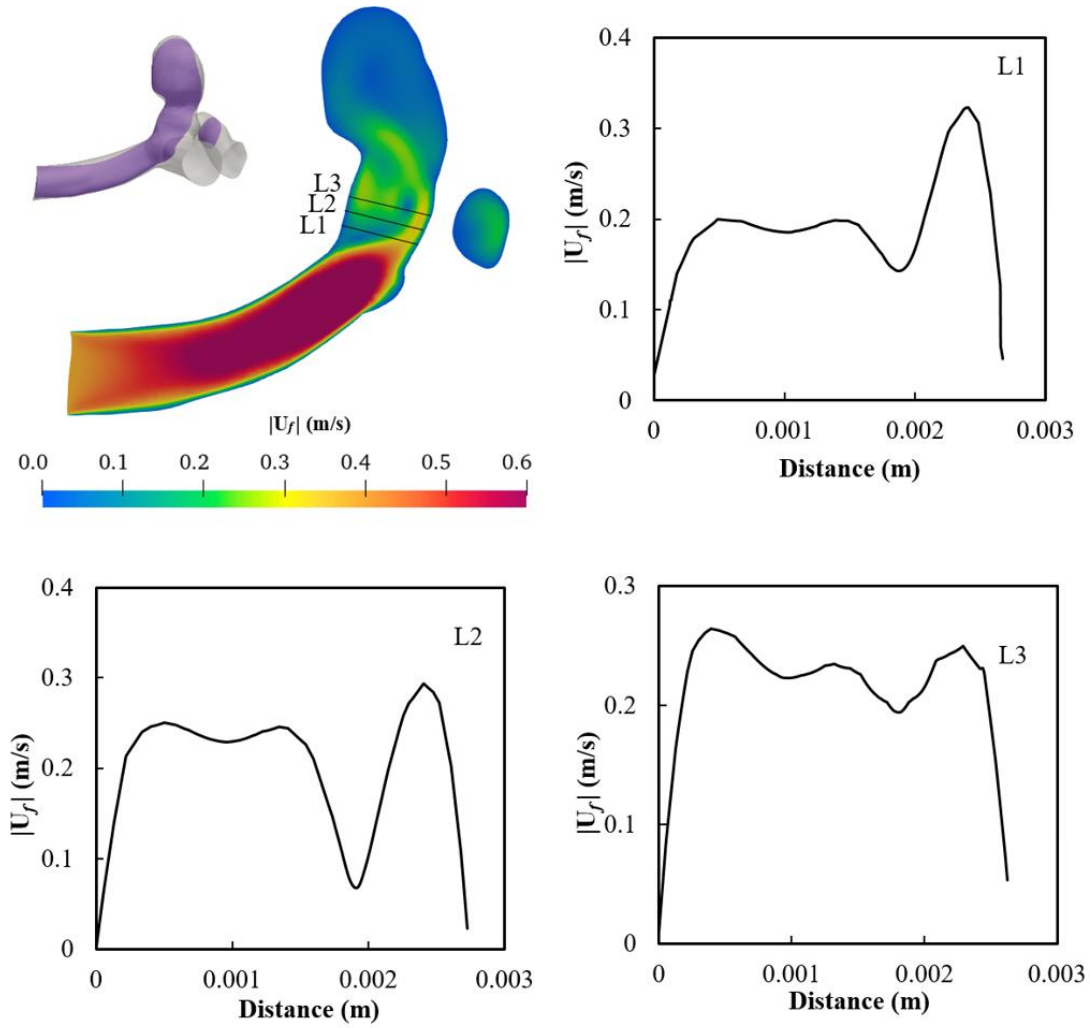

Figure 6.1 : Characteristics of velocity field at the peak systole.

Figure 6.2 shows the contours of the velocity magnitudes at different sections normal to the sac region. It is clear that rapid changes in flow velocities occurs during the different phases of the systole and diastole, and the maximum flow velocity is observed at the peak systole. The magnitude of flow velocity exhibits spatial variations in that

it decreases significantly from the neck to the sac region. Apparently, the rapid changes in the velocity field creates large shearing actions, whose locations move throughout the cardiac cycle. As a result, a very dynamic shear forces are involved, which is expected to degrade the strength of the wall tissues in the dome.

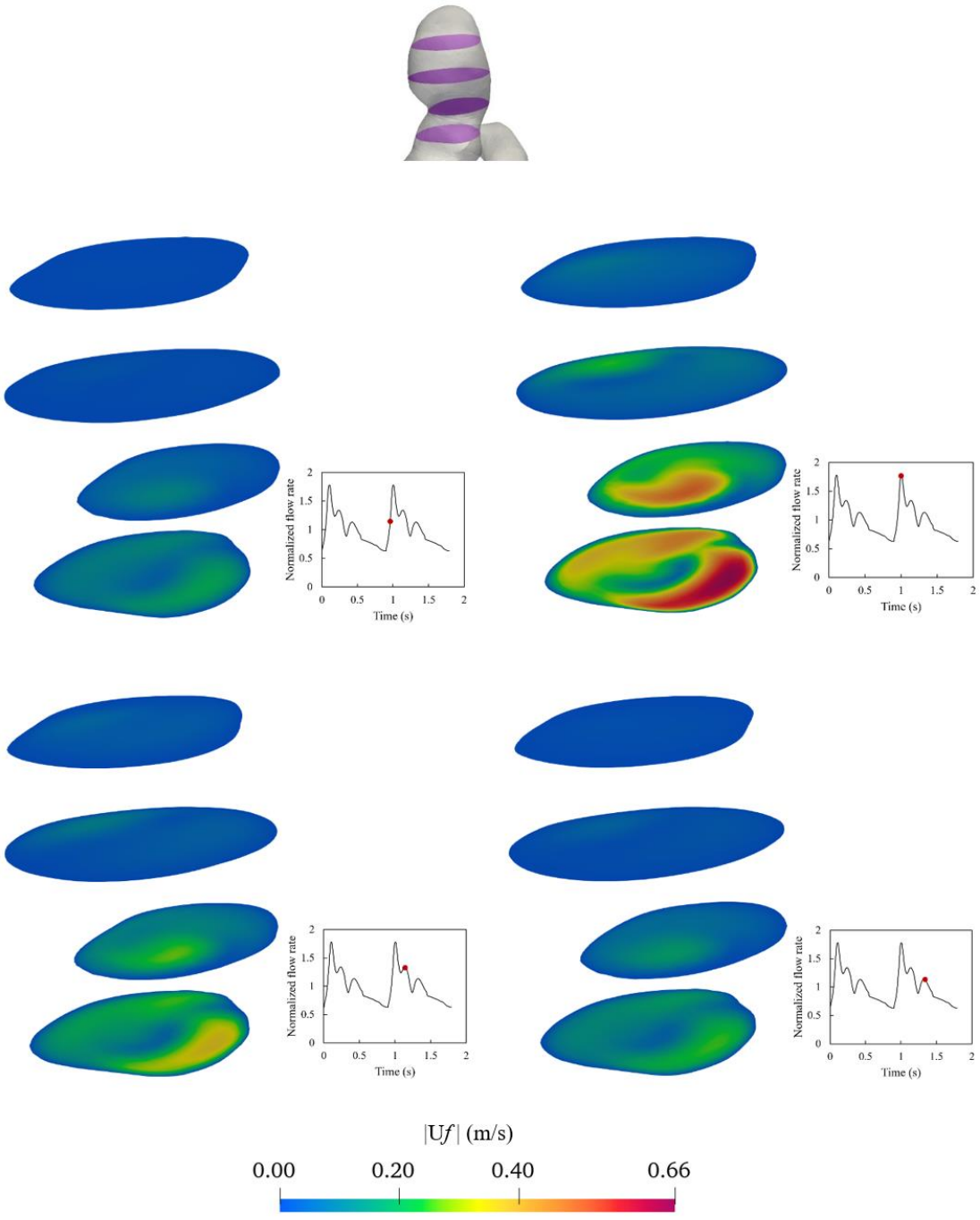

Figure 6.2 : Flow velocities at different times.

6.2 Vortex Structure in the Aneurysm Sac

As it was discussed in the previous chapters, the presence of multiple vortex structures is known as a vital threat in the cerebral aneurysms in that as the number of the vortexes increases so does the rupture risks [58]. Figure 6.3 represents flow streamlines at various phases of the systole. As the inflow velocity achieves its maximum value at the peak systole, the main vortex located at the middle of the sac region was divided

into two interconnecting vortices which indicates that peak systole could be the most dangerous phase for rupture and bleeding (Figure 6.3 b). The vortexes rejoined shortly after the peak systole.

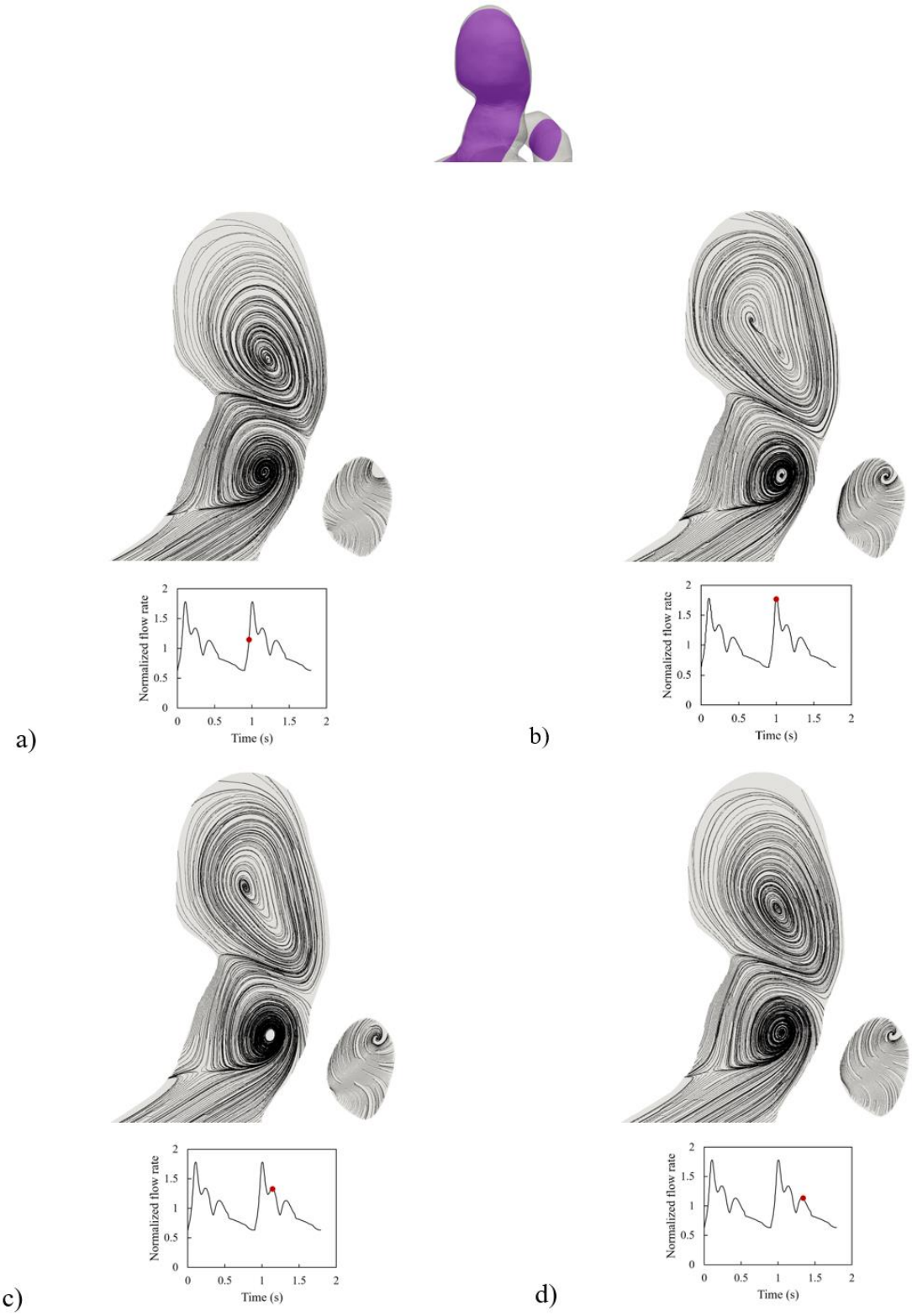

Figure 6.3 : Streamline characteristics at different times.

6.3 von Mises Stresses

We know that the deformations in the wall of a cerebral aneurysm, featured by its displacement, is directly linked with the von Mises stresses. Figure 6.4 clearly shows that the high values of the von Mises stress coincide with the high-OSI but the low-TAWSS values. This actually proves the assertion that the low-TAWSS and the high OSI values are the major hemodynamic parameters to consider in the rupture assessments. In order to quantify this observation, the OSI and von Mises stress values were depicted along the curves, C1 and C2, on the aneurysm wall, and Figure 6.5 reveals that the trends of the OSI and von Mises stresses follow each other very closely.

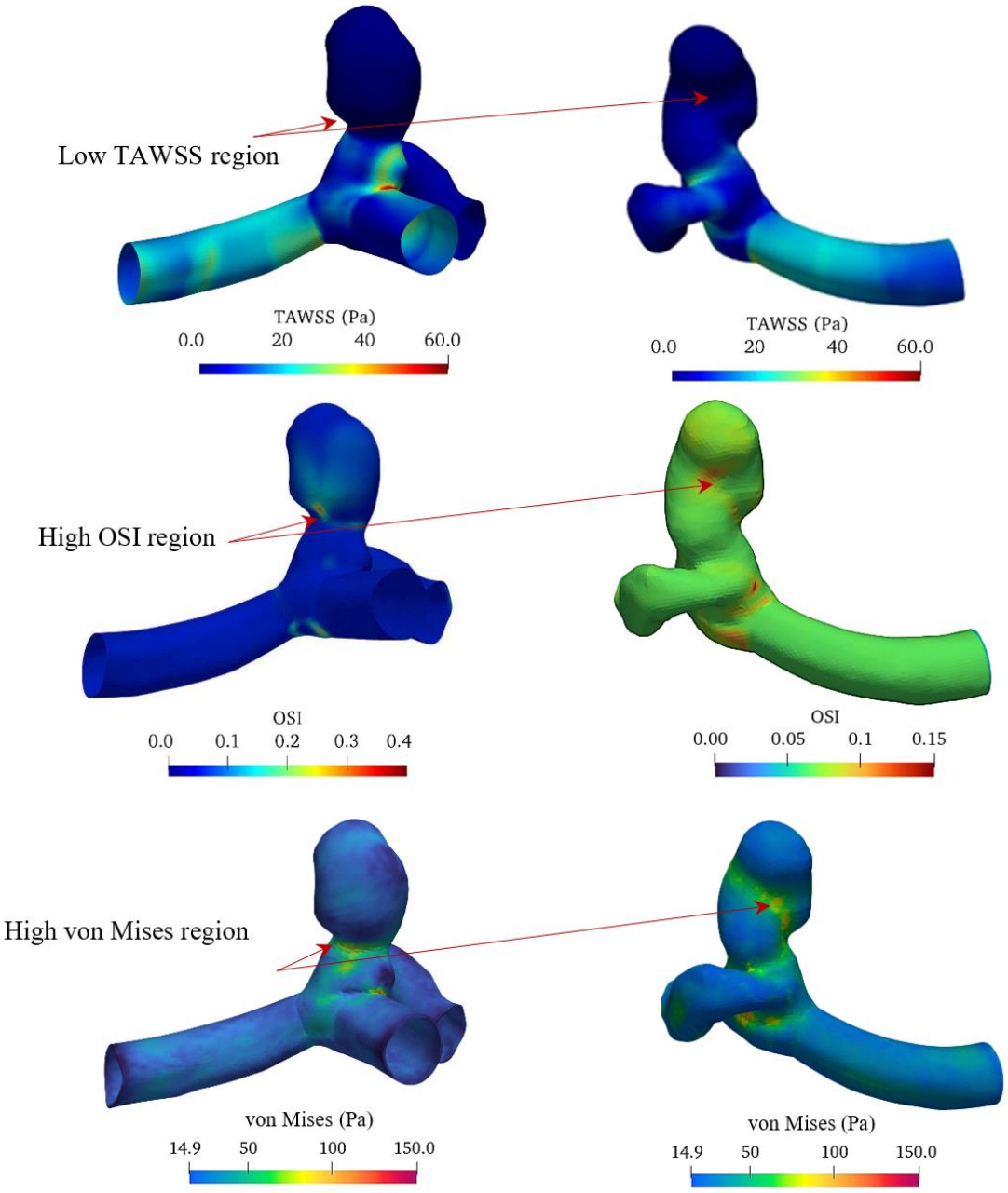

Figure 6.4 : TAWSS, OSI and material parameters for one complete flow cycle.

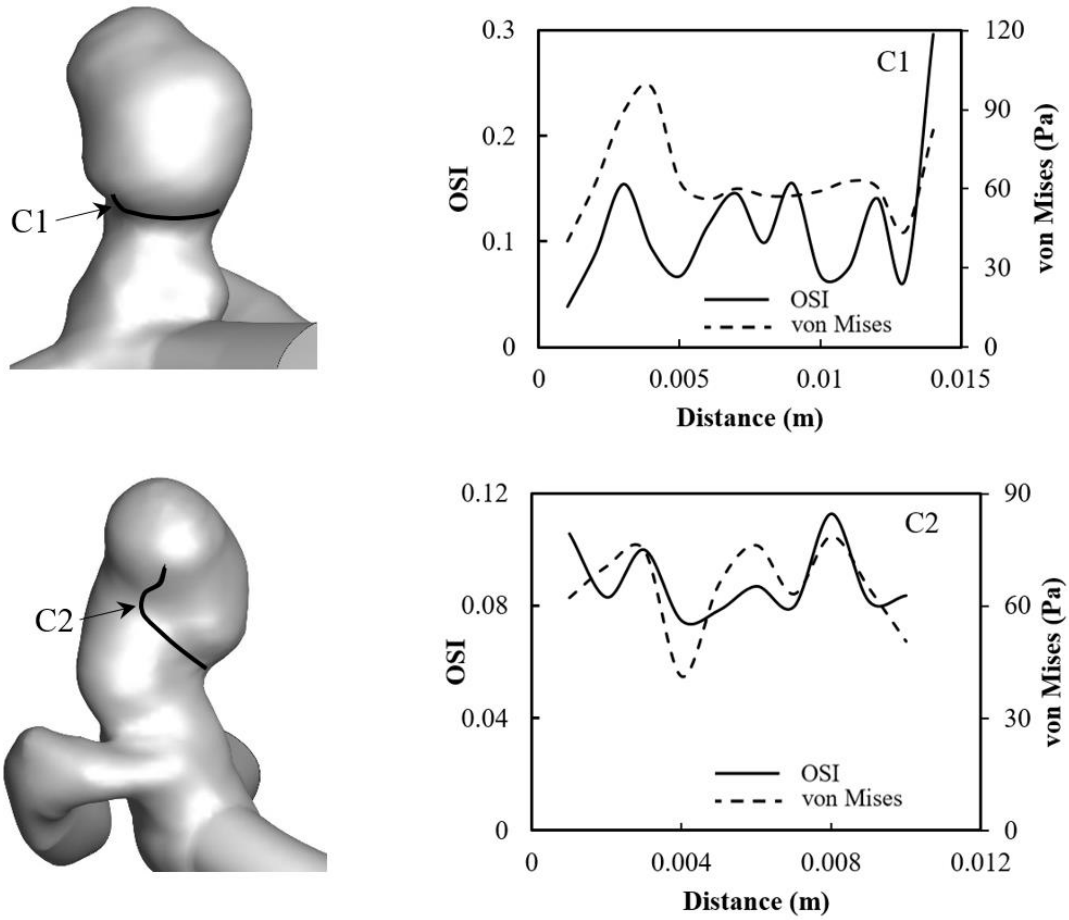

Figure 6.5 : Hemodynamic and material parameters for one complete flow cycle.

6.4 Displacement of Deformable Vessel Wall

Figure 6.6 presents the deformations of the aneurysm dome at different phases of the inflow pulse between the systole and the diastole. It is clear that both the distribution and the magnitude of the displacement vary significantly during the pulsation cycle: The wall displacements become larger as the inflow intensity become higher where the maximum value occurs at the peak systole. The maximum displacement is shown to be an important flow characteristic and mostly occurs in the primary and the secondary impingements zones.

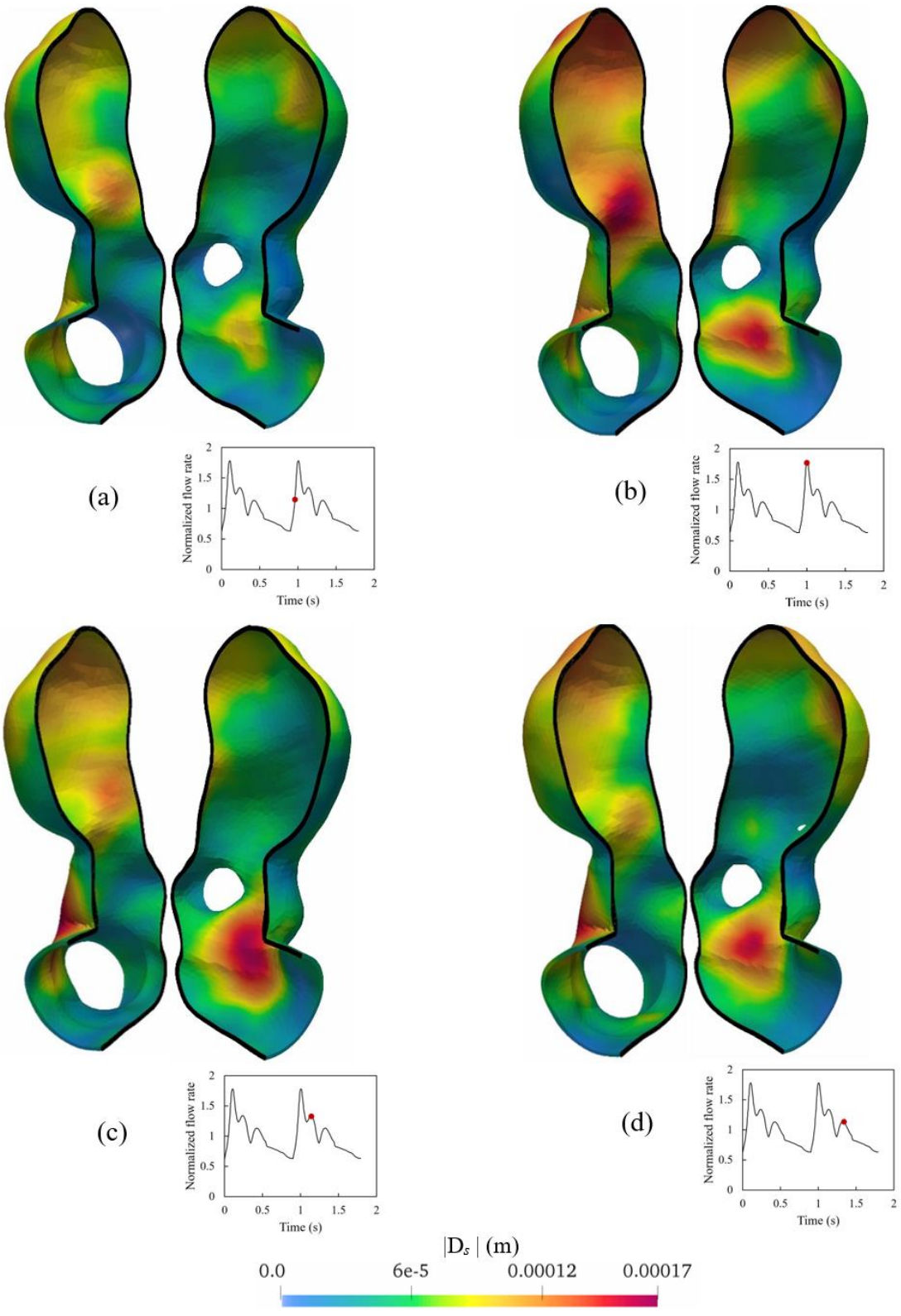

Figure 6.6 : Wall displacements at different times.

7. CONCLUSIONS

A numerical investigation was conducted in order to improve our understanding of flow (e.g., inflow penetration depth, flow complexity, flow impingement zones), wall shear stress based hemodynamic indexes (e.g., OSI and TAWSS) and structure parameters (e.g., von Mises stress) on the rupture risk assessment of cerebral aneurysm.

7.1 Comparison Between Single-phase and Two-phase Blood Flow

The differences in the blood transport with the conventional single-phase approximation and two-phase blood model have been studied and the results were evaluated for the patient-specific aneurysm cases. It was clear that the two-phase simulations seemed to capture many important flow features and, thus, revealed much higher flow complexity compared to the single-phase results. Hence, the two-phase flow portrayed a larger number of unstable flow structures deteriorating the aneurysm risk. It also revealed significantly deeper penetrations into the aneurysm sac than the single-phase model. The hemodynamic indexes based on the wall shear stress showed that the two-phase approach was able to detect very low values of the TAWSS coincided with the areas of high OSI, which were wider than that the single-phase model was disclosed. This indicated that the single-phase analysis could hide the regions at higher risk of rupture. The two-phase approach was also capable of modeling the behavior of the non-Newtonian RBCs suspended in Newtonian plasma. Thus, it showed an apparent potential to enhance the current understanding of the aggregation mechanisms of the RBCs. This could pave the way for the accumulation of the RBCs to be used as the precursor of the thrombus formation. Hence, attempts were made to infer the RBCs aggregation around the concave structures and narrow paths in the saccular aneurysms; the later appeared to be riskier.

7.2 Effects of RBCs Concentration

The effect of variations in the hematocrit level on the blood flow in two cerebral aneurysms was studied using the two-phase Euler-Euler approach and the proper viscosity specifications. The assessment of results has led to the following conclusions:

1) The RBCs aggregation in the aneurysm sac at high hematocrit levels precluded the penetration of the incoming flow and, thus, the inflow depth remained low. At the low end of the H values, however, the maximum inflow jet penetration was achieved, but this led to the vortex formation, possibly to bring into the associated intermittency. As a result, at the marginal blood compositions - extremely high or low H cases - a very weak oxygen supply capacity was anticipated. Besides, when the inflow penetration was large, the momentum exchange due to the rapid diversion of the high-speed inflow at the narrow corners deep inside the aneurysm sac was expected to result in permanent deformations on the walls at the tissue scale.
2) The results also revealed that the hematocrit level had a great influence on the flow instabilities inside the aneurysm dome. At the high H values, the flow complexity was confined in the entrance up to the neck region and, as the H value decreased, the flow became extremely complicated inside the ballooned region. Therefore, the reduction of the H values was anticipated to increase the risk of rupture initiation in those regions.
3) As the hematocrit level decreased to H20, an interesting feature was observed in that an initially single-peaked velocity profile evolved into a double-peak profile. As a result, large gradients occurred near the wall, where the primary inflow was almost stagnant, imposing a high pressure which could deform the walls and increase the likelihood of a secondary aneurysm formation.
4) It was evident that at the low end of the H range, the RBCs' contribution to the WSS happened to be the largest near the neck region, which clearly decreased the possibility of the rapture. The risky zones with the lowest instantaneous WSS were identified in the tip and bleb regions. The TAWSS and OSI indicators were also shown to be dependent on the H values where some drastic changes were observed, in that that a large reduction in hematocrit levels changed an initially low-risk case into a very high rupture risk situation where,

the high OSI values exactly coincided with the low TAWSS values. Nonetheless, the TAWSS values for both patient specific aneurysms were extremely low around the sac region, where very large OSI values were observed.

7.3 FSI Analysis in Cerebral Aneurysm

The movements of the walls of a patient-specific cerebral aneurysm were studied by the analyses of the non-Newtonian blood flow and its interactions with the deformable dome. Upon the evaluation of the present findings, we can make the following deductions:

1) At the peak systole, the inflow achieves its maximum value, which leads to an increase in the number of the vortices and the complexity of the flow in the aneurysm dome. Hence, the peak systole appears to be the most dangerous stage of the cardiac cycle as far as the risk of the rupture and bleeding is concerned.
2) The sharp variations in the flow field during the cardiac cycle generates large shear forces and fluctuations, which deteriorate the wall tissues in the aneurysm dome.
3) Furthermore, the degradation of the uniformity of the flow field leads to the high values of the von Mises stresses, which in turn results in high wall displacements.
4) The maximum values of the von Mises stress nearly coincide with the highest OSI values and these locations overlap with the lowest TAWSS values.
5) The locations of the maximum displacements wander around the surface of the dome, but often remained in the region of the impingement.

REFERENCES

[1] **Grabowski EF**. Thrombolysis, Flow, and Vessel Wall Interactions. J Vasc Interv Radiol 1995;6:25S-29S. https://doi.org/10.1016/S1051-0443(95)71245-3.

[2] **Sforza DM, Putman CM, Cebral JR**. Hemodynamics of cerebral aneurysms. Annu Rev Fluid Mech 2009;41:91–107. https://doi.org/10.1146/annurev.fluid.40.111406.102126.

[3] **Suzuki J, Ohara H**. Clinicopathological study of cerebral aneurysms. J Neurosurg 1978;48:505–14. https://doi.org/10.3171/jns.1978.48.4.0505.

[4] **Brisman JL, Song JK, Newell DW**. Cerebral aneurysms. N Engl J Med 2006;355:928–39. https://doi.org/10.1056/NEJMra052760.

[5] **Clark MG, Wallis MG, Barrett EJ, Vincent MA, Richards SM, Clerk LH, Rattigan S.** Blood flow and muscle metabolism: a focus on insulin action. Am J Physiol Metab 2003;284:E241–58. https://doi.org/10.1152/ajpendo.00408.2002.

[6] **Kornfield TE, Newman EA**. Regulation of Blood Flow in the Retinal Trilaminar Vascular Network. J Neurosci 2014;34:11504–13. https://doi.org/10.1523/JNEUROSCI.1971-14.2014.

[7] **Tohgi H, Yamanouchi H, Murakami M, Kameyama M**. Importance of the hematocrit as a risk factor in cerebral infarction. Stroke 1978;9:369–74. https://doi.org/10.1161/01.STR.9.4.369.

[8] **Brown DW, Giles WH, Croft JB**. Hematocrit and the risk of coronary heart disease mortality. Am Heart J 2001;142:657–63.

[9] **Tamariz LJ, Young JH, Pankow JS, Yeh H-C, Schmidt MI, Astor B, Brancati FL.** Blood Viscosity and Hematocrit as Risk Factors for Type 2 Diabetes Mellitus: The Atherosclerosis Risk in Communities (ARIC) Study. Am J Epidemiol 2008;168:1153–60. https://doi.org/10.1093/aje/kwn243.

[10] **MA JZ, EBBEN J, XIA H, COLLINS AJ**. Hematocrit Level and Associated Mortality in Hemodialysis Patients. J Am Soc Nephrol 1999;10:610–9.

[11] **Di Nisio M, Barbui T, Di Gennaro L, Borrelli G, Finazzi G, Landolfi R.** The haematocrit and platelet target in polycythemia vera. Br J Haematol 2007;136:249–59. https://doi.org/10.1111/j.1365-2141.2006.06430.x.

[12] **Cebral JR, Mut F, Weir J, Putman CM**. Association of Hemodynamic Characteristics and Cerebral Aneurysm Rupture. Am J Neuroradiol 2011;32:264–70. https://doi.org/10.3174/ajnr.A2274.

[13] **Malek AM, Alper SL, Izumo S**. Hemodynamic shear stress and Its sole in atherosclerosis. JAMA 1999;282:2035.

[14] **Atlas SW, Grossman RI, Goldberg HI, Hackney DB, Bilaniuk LT, Zimmerman RA**. Partially thrombosed giant intracranial aneurysms: correlation of MR and pathologic findings. Radiology 1987;162:111–4. https://doi.org/10.1148/radiology.162.1.3786749.

[15] **Jung J, Hassanein A**. Three-phase CFD analytical modeling of blood flow. Med Eng Phys 2008;30:91–103. https://doi.org/10.1016/j.medengphy.2006.12.004.

[16] **Bagchi P, Johnson PC, Popel AS**. Computational fluid dynamic simulation of aggregation of deformable cells in a shear flow. J Biomech Eng 2005;127:1070. https://doi.org/10.1115/1.2112907.

[17] **Das B, Enden G, Popel AS**. Stratified multiphase model for blood flow in a venular bifurcation. Ann Biomed Eng 1997;25:135–53. https://doi.org/10.1007/BF02738545.

[18] **Mori D, Yamaguchi T**. Computational fluid dynamics modeling and analysis of the effect of 3-D distortion of the human aortic Arch. Comput Methods Biomech Biomed Engin 2002;5:249–60. https://doi.org/10.1080/10255840290010698.

[19] **Shojima M**. Magnitude and role of wall shear stress on cerebral aneurysm. Computational fluid dynamic study of 20 middle cerebral artery Aneurysms. Stroke 2004:2500–5. https://doi.org/10.1161/01.STR.0000144648.89172.of.

[20] **Dormandy JA**. Clinical significance of blood viscosity. Ann R Coll Surg Engl 1970;47:211–28.

[21] **Eckmann DM, Bowers S, Stecker M, Cheung AT**. Hematocrit, volume expander, temperature, and shear rate effects on blood viscosity. Anesth Analg 2000;91:539–45. https://doi.org/10.1213/00000539-200009000-00007.

[22] **Jung JM, Lee DH, Kim KT, Choi MS, Cho YG, Lee HS, Choi SI, Kim DS.** Reference intervals for whole blood viscosity using the analytical performance-evaluated scanning capillary tube viscometer. Clin Biochem2014;47:489–93. https://doi.org/10.1016/j.clinbiochem.2014.01.021.

[23] **Srivastava LM, Srivastava VP**. Peristaltic transport of blood: Casson model—II. J Biomech 1984;17:821–9. https://doi.org/10.1016/0021-9290(84)90140-4.

[24] **Jung J, Hassanein A, Lyczkowski RW**. Hemodynamic Computation Using Multiphase Flow Dynamics in a Right Coronary Artery. Ann Biomed Eng 2006;34:393–407. https://doi.org/10.1007/s10439-005-9017-0.

[25] **Michler C, Hulshoff SJ, van Brummelen EH, de Borst R**. A monolithic approach to fluid–structure interaction. Comput Fluids 2004;33:839–48. https://doi.org/10.1016/j.compfluid.2003.06.006.

[26] **Causin P, Gerbeau JF, Nobile F**. Added-mass effect in the design of partitioned algorithms for fluid–structure problems. Comput Methods Appl Mech Eng 2005;194:4506–27.

[27] **Sotiropoulos F, Yang X**. Immersed boundary methods for simulating fluid–structure interaction. Prog Aerosp Sci 2014;65:1–21.

[28] **Hirt C., Amsden A., Cook J.** An arbitrary Lagrangian-Eulerian computing method for all flow speeds. J Comput Phys 1974;14:227–53. https://doi.org/10.1016/0021-9991(74)90051-5.

[29] **Cardiff P, Tuković Ž, Jasak H, Ivanković A**. A block-coupled Finite Volume methodology for linear elasticity and unstructured meshes. Comput Struct 2016;175:100–22. https://doi.org/10.1016/j.compstruc.2016.07.004.

[30] **Tuković Ž, Karač A, Cardiff P, Jasak H, Ivanković A**. OpenFOAM Finite Volume Solver for Fluid-Solid Interaction. Trans FAMENA 2018;42:1–31. https://doi.org/10.21278/TOF.42301.

[31] **Gatzhammer B, Mehl M, Neckel T**. A coupling environment for partitioned multiphysics simulations applied to fluid-structure interaction scenarios. Procedia Comput Sci 2010;1:681–9. https://doi.org/10.1016/j.procs.2010.04.073.

[32] **Bungartz H-J, Lindner F, Gatzhammer B, Mehl M, Scheufele K, Shukaev A, Uekerman B.** preCICE – A fully parallel library for multi-physics surface coupling. Comput Fluids 2016;141:250–8. https://doi.org/10.1016/j.compfluid.2016.04.003.

[33] **Rodenberg B, Desai I, Hertrich R, Jaust A, Uekermann B**. FEniCS–preCICE: Coupling FEniCS to other simulation software. SoftwareX 2021;16:100807. https://doi.org/10.1016/j.softx.2021.100807.

[34] **Degroote J, Bathe K, Vierendeels J**. Performance of a new partitioned procedure versus a monolithic procedure in fluid–structure interaction. Comput Struct 2009;87:793–801. https://doi.org/10.1016/j.compstruc.2008.11.013.

[35] **Irons BM, Tuck RC**. A version of the Aitken accelerator for computer iteration. Int J Numer Methods Eng 1969;1:275–7. https://doi.org/10.1002/nme.1620010306.

[36] **Küttler U, Wall WA**. Fixed-point fluid–structure interaction solvers with dynamic relaxation. Comput Mech 2008;43:61–72. https://doi.org/10.1007/s00466-008-0255-5.

[37] **Scheufele K**. Robust Quasi-Newton Methods for Partitioned Fluid-Structure Simulations 2015. https://doi.org/10.13140/RG.2.2.28442.08648.

[38] **Enwald H, Peirano E, Almstedt A-E**. Eulerian two-phase flow theory applied to fluidization. Int J Multiph Flow 1996;22:21–66.

[39] **Hill DP**. The Computer Simulation of Dispersed Two-phase Flows. Grad Thesis 1998.

[40] **Basset AB**. A treatise on hydrodynamics, Vol. 1 by A. B. Basset 1888.

[41] **Schiller L, Naumann Z**. A drag coefficient correlation. VDI Zeitung 1935;77:318–20.

[42] **Kanitz M, Grabe J**. The influence of the void fraction on the particle migration: A coupled computational fluid dynamics–discrete element method study about drag force correlations. Int J Numer Anal Methods Geomech 2021;45:45–63. https://doi.org/10.1002/nag.3131.

[43] **Gijsen FJH, Allanic E, van de Vosse FN, Janssen JD**. The influence of the non-Newtonian properties of blood on the flow in large arteries: unsteady flow in a 90° curved tube. J Biomech 1999;32:705–13. https://doi.org/10.1016/S0021-9290(99)00014-7.

[44] **Shaaban AM, Duerinckx AJ**. Wall shear stress and early atherosclerosis. Am J Roentgenol 2000;174:1657–65. https://doi.org/10.2214/ajr.174.6.1741657.

[45] **Pinto SIS, Campos JBLM**. Numerical study of wall shear stress-based descriptors in the human left coronary artery. Comput Methods Biomech Biomed Engin 2016;19:1443–55. https://doi.org/10.1080/10255842.2016.1149575.

[46] **Caro CG, Fitz-Gerald JM, Schroter RC**. Atheroma and arterial wall shear - Observation, correlation and proposal of a shear dependent mass transfer mechanism for atherogenesis. Proc R Soc London Ser B Biol Sci 1971;177:109–33. https://doi.org/10.1098/rspb.1971.0019.

[47] **Paszkowiak JJ, Dardik A**. Arterial Wall Shear Stress: Observations from the Bench to the Bedside. Vasc Endovascular Surg 2003;37:47–57. https://doi.org/10.1177/153857440303700107.

[48] **Zhang Y, Tian Z, Jing L, Zhang Y, Liu J, Yang X**. Bifurcation type and larger Low Shear area are associated with rupture status of very small intracranial aneurysms. Front Neurol 2016;7:1–6. https://doi.org/10.3389/fneur.2016.00169.

[49] **He X, Ku DN**. Pulsatile flow in the human left coronary artery bifurcation: average conditions. J Biomech Eng 1996;118:74–82. https://doi.org/10.1115/1.2795948.

[50] **Miura Y, Ishida F, Umeda Y, Tanemura H, Suzuki H, Matsushima S, Shimosaka S, Taki W.** Low wall shear stress Is independently associated with the rupture status of middle cerebral artery aneurysms. Stroke 2013;44:519–21. https://doi.org/10.1161/STROKEAHA.112.675306.

[51] **Ishida F, Tsuji M, Tanioka S, Tanaka K, Yoshimura S, Suzuki H**. Computational fluid dynamics for cerebral aneurysms in clinical settings. Acta Neurochir. Suppl., vol. 132, 2021, p. 27–32. https://doi.org/10.1007/978-3-030-63453-7_4.

[52] **Ford MD, Alperin N, Lee SH, Holdsworth DW, Steinman DA**. Characterization of volumetric flow rate waveforms in the normal internal carotid and vertebral arteries. Physiol Meas 2005;26:477–88. https://doi.org/10.1088/0967-3334/26/4/013.

[53] **Dhondt G**. Method for Three-dimensional Method for Three-dimensional Thermomechanical Applications. John Wiley & Sons; 2004.

[54] **Karino T, Goldsmith HL**. Flow behaviour of blood cells and rigid spheres in an annular vortex. Philos Trans R Soc London B, Biol Sci 1977;279:413–45. https://doi.org/10.1098/rstb.1977.0095.

[55] **Weller HG, Tabor G, Jasak H, Fureby C**. A tensorial approach to computational continuum mechanics using object-oriented techniques. Comput Phys 1998;12:620. https://doi.org/10.1063/1.168744.

[56] **Ferziger JH, Perić M, Street RL**. Computational Methods for Fluid Dynamics. vol. 5. Cham: Springer International Publishing; 2020. https://doi.org/10.1007/978-3-319-99693-6.

[57] **Cebral JR, Mut F, Raschi M, Scrivano E, Ceratto R, Lylyk P, Putman CM.** Aneurysm Rupture Following Treatment with Flow-Diverting Stents: Computational Hemodynamics Analysis of Treatment. Am J Neuroradiol 2011;32:27–33. https://doi.org/10.3174/ajnr.A2398.

[58] **Cebral JR, Castro MA, Burgess JE, Pergolizzi RS, Sheridan MJ, Putman CM**. Characterization of cerebral aneurysms for assessing risk of rupture by using patient-specific computational hemodynamics models. AJNR Am J Neuroradiol 2006;26:2550–9. https://doi.org/10.1016/S0098-1672(08)70473-9.

[59] **Sugiyama S-I, Endo H, Omodaka S, Endo T, Niizuma K, Rashad S, Nakayama T, Funamoto K, Ohta M, Tominaga T.** Daughter Sac Formation Related to Blood Inflow Jet in an Intracranial Aneurysm. World Neurosurg 2016;96:396–402. https://doi.org/10.1016/j.wneu.2016.09.040.

[60] **Kawaguchi T, Nishimura S, Kanamori M, Takazawa H, Omodaka S, Sato K, Maeda N, Yokoyama Y, Midorikawa H, Sasaki T, Nishijima M.** Distinctive flow pattern of wall shear stress and oscillatory shearindex: similarity and dissimilarity in ruptured and unruptured cerebral aneurysm blebs. JNeurosurg2012;117:774–80. https://doi.org/10.3171/2012.7.JNS111991.

[61] **Brindise MC, Rothenberger S, Dickerhoff B, Schnell S, Markl M, Saloner D, Rayz VL.** Multi-modality cerebral aneurysm haemodynamic analysis: in vivo 4D flow MRI, in vitro volumetric particle velocimetry and in silico computational fluid dynamics. J R Soc Interface 2019;16:20190465. https://doi.org/10.1098/rsif.2019.0465.

CURRICULUM VITAE

Name Surname **:** Hamed PAHLAVANI

EDUCATION :

- **B.Sc.** **:** 2008, Azad University of Khoy, Faculty of Engineering, Mechanical Engineering Department
- **M.Sc.** **:** 2015, ITU, Faculty of Mechanical Engineering.

PUBLICATIONS, PRESENTATIONS AND PATENTS ON THE THESIS:

- **Pahlavani H.,** Özdemir İB., Yıldırım. D. 2022. CFD Models for Aneurysm Analyses and Their Use in Identifying Thrombosis Formation and Risk Assessment, Journal of Mechanics in Medicine and Biology.
- **Pahlavani H.,** Özdemir İB. 2022. Numerical Investigation of the Effects of Two-Phase Blood Flow and its Hemodynamic Characteristics on the Rupture of Cerebral Aneurysm, International Conference on Research in Applied Sciences, April 22-24, 2022 Antalya, Turkey.